Upconversion and Near Infrared Spectroscopy of Erbium doped Calcium Sulfide

by

Steven Patrick Compton

(Under the direction of Uwe Happek)

Abstract

This dissertation details the fabrication process and spectroscopic characterization of erbium doped calcium sulfide as a tool for medical research and treatment. The use of this material in the medical field as a consequence of its upconversion properties is reviewed, and a critical review of its advantages and limitations is given.

Index words: Calcium Sulfide, Trivalent Erbium, CaS, Er^{3+}, Upconversion, Luminescence, Condensed Matter Physics, Photoactivator, Dissertations (academic)

Upconversion and Near Infrared Spectroscopy of Erbium doped Calcium Sulfide

by

Steven Patrick Compton

B.S., The University of Georgia, 2003

A Dissertation Submitted to the Graduate Faculty
of The University of Georgia in Partial Fulfillment
of the
Requirements for the Degree

Doctor of Philosophy

Athens, Georgia

2009

Upconversion and Near Infrared Spectroscopy of Erbium doped Calcium Sulfide

by

Steven Patrick Compton

Approved:

Major Professor: Uwe Happek

Committee: Bill Dennis
Heinz-Bernd Schüttler

Electronic Version Approved:

Maureen Grasso
Dean of the Graduate School
The University of Georgia
December 2009

Dedication

To my wife and family who have shown me patience and understanding for so many years. I love you so much! Rosana, your support has made me strong and given me the inspiration to succeed.

Acknowledgments

I would like to thank all of my past and present teachers, advisors, and committee members who have helped me to develop and learn the skills necessary to succeed in the world. Of special mention is Dr. Uwe Happek who has served as all three of those roles in my life. Without his encouragement and enthusiasm for science I never would have gotten this far.

I would also like to thank the past and present group members and classmates. Everyone I have ever worked with has had an influence on me and therefore this work. The entire Physics and Astronomy department here at the University of Georgia has been critical to the success of everyday operations, which includes my own education and research. I appreciate their much needed support. Finally, I would like to thank all of my students over the years for forcing me to constantly look at things with fresh eyes.

Table of Contents

List of Figures

List of Tables

List of Abbreviations

CCD	Charge Coupled Device
CW	Continuous Wave
EDFA	Erbium Doped Fiber Amplifier
ESA	Excited State Absorption
ET	Energy Transfer
FFT	Fast Fourier Transform
FTIR	Fourier Transform Infrared
GSA	Ground State Absorption
LMCT	Ligand to Metal Charge Transfer
NIR	Near Infrared
PA	Photon Avalanche
PL	Photoluminescence
PMT	Photomultiplier Tube
UC	Upconversion
UHV	Ultra High Vacuum
UV	Ultraviolet
XRD	X-Ray Diffraction

Chapter 1

Introduction

Erbium doped materials are widely studied due to their unique properties. Erbium is used for a variety of uses, from nuclear fuel rods to pink ceramics and jewelry [1]. Applications that require upconversion (medical imaging) and near infrared (NIR) emission (optical amplifiers) generate the most interest.

Upconversion involves the conversion of two or more low energy photons into one photon of higher energy, often converting NIR light into visible (VIS) or even ultra-violet (UV) light. Erbium's "ladder"-like energy levels from $f-f$ transitions allow several possible upconversion schemes.

In the biological and medical fields, thiol (-SH) functional groups (an extension of a molecule which contains a sulfur atom attached to a hydrogen atom by a single covalent bond) are often used to combine molecular "tools" like fluorescent markers, nanoparticles, proteins, DNA, or even microelectromechanical systems to each other. Antibodies (protein which can identify foreign objects such as viruses and bacteria in the body) could be conjugated with photoactivated toxins designed to destroy the foreign object. This research is limited by the mismatch between the required photoactivation wavelength (usually in the VIS to UV region) and the range of minimal absorbency in the human body (between 700 nm and 900 nm) [2, 3].

If irradiated at a wavelength between 700 nm and 900 nm, an erbium doped system could convert the NIR photons via upconversion to higher energy photons more suitable for photoactivated toxins. A sulfide containing inorganic crystal host lattice provides an easy means of connecting the erbium system to the toxin and antibody through the use of thiol

functional groups. Erbium doped materials have already been used to observe upconversion fluorescence imaging *in vivo* to a tissue depth of 10 mm [4].

While erbium is one of the most commonly used of the lanthanides for upconversion, by far its most groundbreaking and widespread use is for optical amplifiers in the telecommunications industry. Characteristic emission in the 1.5 μm range makes it a perfect candidate for telecommunications technologies which operate over the range of 1530 nm to 1565 nm [5–8].

Sulfide systems, like bromides, chlorides, and iodides are also known to be low phonon energy materials [9]. While interest in erbium's 1.5 μm emission line is widespread for telecommunications and lasing systems, the low energy transition is highly prone to non radiative decay by multiphonon relaxation. The use of a low phonon energy material which would decrease the probability of non radiative decay is promising.

Sulfide hosts have received much less attention due to the hygroscopic nature of sulfide materials and the corresponding limitations encountered in the fabrication process. This study attempts to minimize those limitations by choosing calcium as the group II ionic pair to sulfur. Other alkaline earth metals, like barium or magnesium, are much more hygroscopic when paired with sulfur.

This work will investigate erbium doped calcium sulfide and its spectroscopic properties related to upconversion and NIR emission. First, some background on upconversion will be presented. The upconversion chapter is intended to give the reader the essential details that are important with respect to this work. Next, some background on erbium doped calcium sulfide and previous work on related systems performed by other groups will be examined. The fabrication process of the phosphor will be given in chapter four, with structure confirmation via an x-ray diffraction study. The subsequent two chapters will explain methods and discuss results of spectroscopic analysis related to upconversion and NIR photoluminescent emission properties. The final chapter will give conclusions and provide strategies for future research.

Chapter 2

Upconversion

Upconversion is an optical process by which lower energy photons can be converted into higher energy photons. To satisfy energy conservation laws, multiple low energy photons are required to create a single photon of higher energy. Multi-photon processes are common in many areas of scientific research. Second, third, and fourth harmonic generation, for example, are often used to shift the output frequency for Nd:YAG lasers. Two-photon laser microscopy is a well established technique used in the field of biology and is based on a nonlinear process where two identical photons are *simultaneously* absorbed to excite an ion whose energy gap is two times the amount of energy provided by only one of the photons. Upconversion (UC), however, is defined as a *sequential* process and can be observed using much lower excitation intensities (see figure 2.1).

Upconversion was first proposed by N. Bloembergen in 1959 [10] as a method for counting infrared (IR) photons. This proposal by Bloembergen came right on the heels of Förster's [11] and Dexter's [12] landmark papers on theoretical non radiative energy transfer and sensitized luminescence. These three papers laid the ground work for all future upconversion research. Confirmation of upconversion in Er^{3+}followed in 1966, shortly after the advent of the laser, by several different groups including Auzel [13–15] in France, and Ovsyanki and Feofilov [16, 17] in the Soviet Union. There are three generally accepted upconversion mechanisms; excited state absorption (ESA) upconversion, energy transfer (ET) upconversion, and photon avalanche (PA) upconversion [18–20].

2.1 Excited State Absorption

Upconversion from excited state absorption (ESA), also referred to as sequential absorption upconversion, is the prevalent mechanism for samples with low dopant ion concentrations simply because of the high probability that upconversion ions are isolated from each other. This isolation prevents energy transfers between ions leading to other types of upconversion, which will be discussed later. Disregarding energy transfers, ESA can be modeled by a simple three level system, as seen in figure 2.1. State 1, or $|1\rangle$, is the lowest energy state and is often the ground state. State 2, or $|2\rangle$, is a metastable state, preferably with a long lifetime, and state 3, or $|3\rangle$, is the excited state which, upon decay to $|1\rangle$, allows emission of an upconversion photon.

The first step of ESA upconversion is referred to as the ground state absorption (GSA) step. It requires a photoexcitation source, which we will call source "a" that contains photons which have the right amount of energy to excite the ion from $|1\rangle$ to $|2\rangle$ (i.e. $h\nu_a = \Delta E_{21}$). A second photon from a different source "b" may then excite the ion up to $|3\rangle$. As with the GSA transition, ESA requires $h\nu_b = \Delta E_{32}$. The longer the lifetime* of $|2\rangle$, the larger the probability that this ion will be excited by a second source ("b") up to $|3\rangle$. Once the ion reaches $|3\rangle$, radiative decay can occur from $|3\rangle$ to $|1\rangle$ which results in a photon emission of energy equal to $h(\nu_a + \nu_b)$. The length of the metastable state lifetime, τ_2, and its influence on the effectiveness of the process can be explained mathematically.

Using a macroscopic approach, we can establish the rate equations for $|1\rangle$, $|2\rangle$, and $|3\rangle$ as

$$\frac{dn_1}{dt} = W_A(n_2 - n_1) + W_{21}n_2 + W_{31}n_3 \tag{2.1}$$

$$\frac{dn_2}{dt} = W_B(n_3 - n_2) + W_A(n_1 - n_2) + W_{32}n_3 - W_{21}n_2 \tag{2.2}$$

and

*For rare earth ions, the level 2 lifetime is typically 1 - 10 ms.

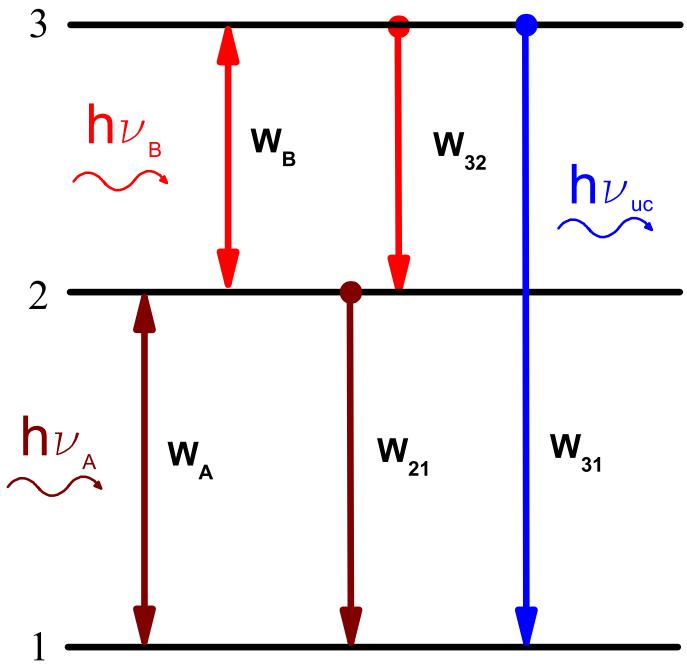

Figure 2.1: Energy level diagram depicting the ESA upconversion mechanism for a three level system. Absorption and stimulated emission are represented by two directional arrows.

$$\frac{dn_3}{dt} = W_B(n_2 - n_3) - W_{32}n_3 - W_{31}n_3 \tag{2.3}$$

The pump rate coefficient can be defined, using W_A as an example, by the following...

$$W_A = \left[\frac{\sigma_{12}I_A}{h\nu_A}\right] \tag{2.4}$$

where W_{12} is the pump rate coefficient from state 1 to state 2, σ_{12} is the absorption cross section for the $1 \rightarrow 2$ transition, I_a is the photon pump intensity of source "a," and $h\nu_a$ is the photon energy related to source "a." It should also be said that the population densities of the three levels are normalized such that

$$n_1 + n_2 + n_3 = 1 \tag{2.5}$$

The response of the mechanism in terms of upconverted photoluminescent intensity is related to the population density of $|3\rangle$ and the relaxation rate coefficient W_{31}. From the steady state form of the equations above we can solve for n_3 to get the following relationship.

$$n_3 = \frac{W_A W_B}{3W_A W_B + 2W_A W_{31} + 2W_A W_{32} + W_B W_{21} + W_B W_{31} + W_{31} W_{21} + W_{32} W_{21}} \tag{2.6}$$

If we allow $\Delta E_{21} = \Delta E_{32}$, we may use the same source for both GSA and ESA states. This simplification has its basis in real world scenarios and is true for the case of CaS:Er^{3+}. In addition, we can extract the excitation intensity term from the pump rate coefficients W_A and W_B, by defining two new terms $W'_A = W_A/I$ and $W'_B = W_B/I$ such that

$$n_3 = \frac{(W'_A W'_B)I^2}{(3W'_A W'_B)I^2 + (2W'_A W_{31} + 2W'_A W_{32} + W'_B W_{21} + W'_B W_{31})I + (W_{31} W_{21} + W_{32} W_{21})} \tag{2.7}$$

In the denominator we see an I^2 dependent, an I dependent, and an I independent term. Since we expect the spontaneous emission rate to be much larger than the stimulated

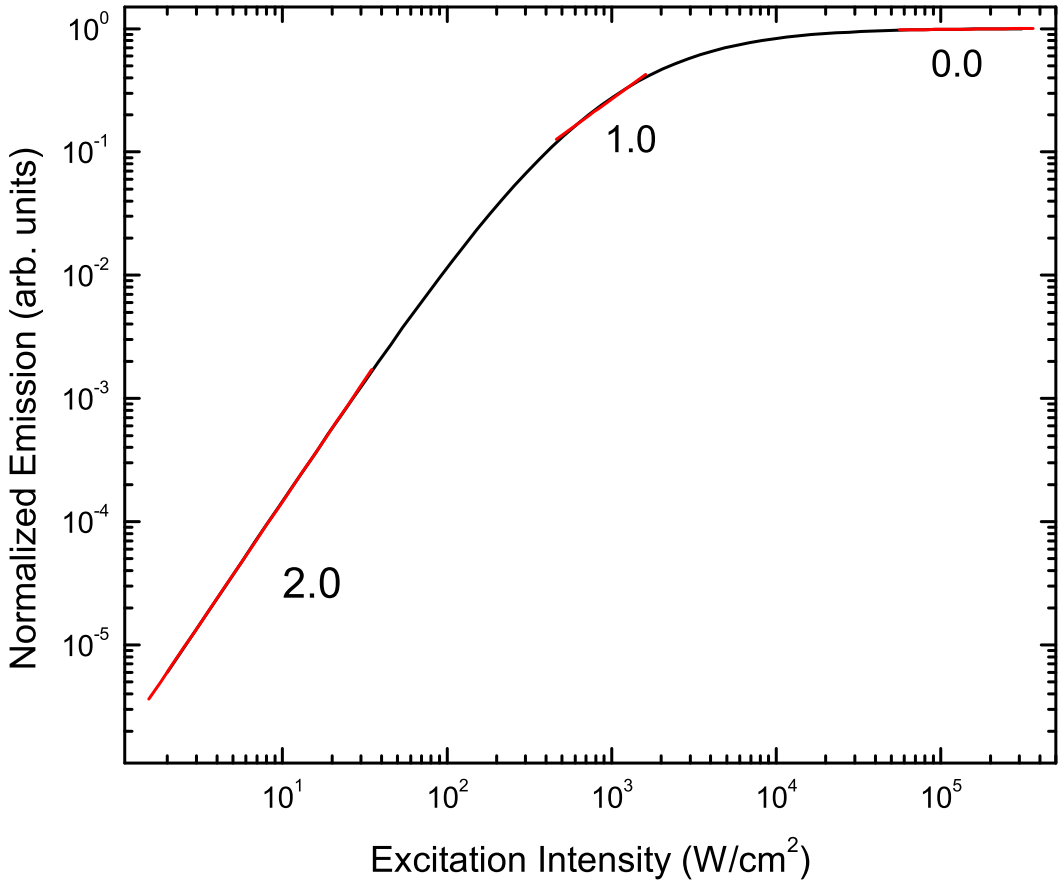

Figure 2.2: Theoretical emission intensities for ESA upconversion as a function of excitation intensity. Regions of I^2 dependence, I dependence, and I independence are labeled by their slopes of 2.0, 1.0, and 0.0 respectively. Plot is based on equation (2.7) and the following material properties: W_{21}=W_{31}=W_{32}=$W_A/1000$=$W_B/1000$.

emission rate, the I independent term dominates at low intensities [21]. As the intensity increases we see a total of three different regimes.

The first regime corresponds to a large population density in the ground state, hence $n_1 \approx 1$. As a result, $n_3 \propto I^2$. As the excitation intensity increases, the influence of the I dependent term increases such that $n_3 \propto I^2/I = I$. This second regime corresponds to a saturation of the metastable state $|2\rangle$ such that $n_1 \approx n_2$. Continuing to increase I will establish a limit where $n_1 = n_2 = n_3 = 1/3$ and the I^2 dependent term dominates over the other two terms in the denominator.

In the low intensity regime there is a more general rule that for an n photon process, the upconverted emission is proportional to I^n. Therefore, the observation of the I dependence in the low intensity regime is useful for establishing the number of photons required for a given process. If emission intensity is plotted as a function of excitation intensity on a log-log scale, the slope of the plotted data corresponds to the number of photons required for the process.

2.2 Energy Transfer Upconversion

Energy transfer processes (ETs) between ions give rise to several possible mechanisms which expand on the ESA process. They can also introduce unwanted quenching effects which lead to non radiative relaxation. The energy transfer may occur between two of the same ions (as seen in Er^{3+}) [22, 23] or between two different ions (commonly seen in Yb^{3+}/Er^{3+}co-doped samples) [24–29].

The *sensitizer* (energy donor) is the ion which is promoted by the excitation source. The *activator* (energy acceptor) receives the energy transferred from the sensitizer. Some papers refer to sensitizers and activators as donors and acceptors, however, these terms will be avoided.

As stated earlier, ESA is prevalent in doped samples with low concentrations of a single upconverting ion. If the concentration of dopant ions increases sufficiently[†], or a second dopant is added, we start to observe transfers which lead to upconversion mechanisms as depicted in figure 2.3. The energy transitions for each ion are equal in the case of resonant energy transfer, or can differ by an amount $\sim k_B T$ for phonon assisted, non-resonant energy transfer [30].

Under ET upconversion, the excitation source acts on the sensitizer. Multiple energy transfer events are used to climb the energy level "ladder" of the activator until it reaches an excited state that leads to upconversion. In the case of Yb^{3+}/Er^{3+} co-doped samples, Yb^{3+} is used to harvest pump source energy, while the Er^{3+} energy levels provide the "ladder" that leads to upconversion emission.

Under this scenario, multiple sensitizers feed energy to each activator, thus allowing increased efficiency even at low activator concentrations. Alternatively, both activator and sensitizer concentrations can be minimized in the unique situation where the activator and sensitizer substitute in different but proximal sites within the host lattice. This enables a clustering effect which would maintain a small activator/sensitizer distance regardless of concentration [31–33]. It should be noted that this technique diminishes the effects of energy migration (also referred to as dispersion) along with its positive and negative effects[‡].

An analysis of sequential energy transfers from a sensitizer to an activator by Auzel can be compared to our ESA model in the following way [20]. The rate of promotion of a single ion from the ground state to second excited state $|3\rangle$ defined as W_{13}. In the ESA model, W_{13} is equal to the product of the two absorption rates.

$$W_{13} = W_A \cdot W_B \tag{2.8}$$

[†]Förster gives the probability of such a transfer as $\sim R^{-6}$ [11]

[‡]...positive, if migration of energy leads ultimately to an activator...negative, if energy migration leads to quenching

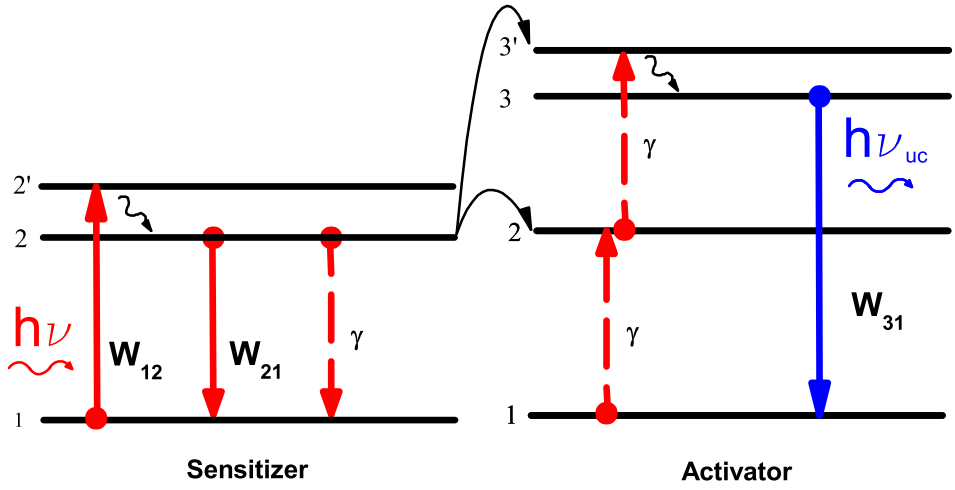

Figure 2.3: Energy level diagram depicting the ET upconversion mechanism for a two level system (the sensitizer) feeding a four level system (the activator). Photoexcitation transitions and ground state relaxations are indicated by solid red and blue lines, while energy transfer transitions are represented by dashed lines. Solid black lines correspond to nonradiative relaxations.

In the ET model provided by Auzel, the promotion rate W_{13} is the product of two energy transfers and the concentration of excited sensitizers capable of such a transfer. The concentration of excited sensitizers is the product of the total concentration of sensitizers, n_S, and the absorption rate, W_A. Therefore, the promotion rate is ultimately influenced by the number of sensitizers, the absorption rate for the sensitizers, and the energy transfer rate from sensitizer to activator, W_{SA}, according to the following.

$$W_{13} = W_A^2 \cdot W_{SA}^2 \cdot n_S^2 \tag{2.9}$$

Overall, the behavior for ET upconversion and ESA upconversion is similar. At high excitation intensities, saturation of the activator excited states will result in an equilibrium between the activator and the sensitizer, where energy is just as likely to be transfered back to the sensitizer. As the excitation intensity is increased, the intensity of upconverted photoluminescence will remain the same, just like the saturated ESA regime. At low intensities, the ET emission is proportional to I^2 as in the case of ESA. But with ET, n_3 is populated at a different rate, influenced by a factor of $n_S^2 \cdot W_{SA}^2$.

2.3 Photon Avalanche Upconversion

In the previous section we saw how a single excitation source could be used for GSA transitions, while supporting energy transfers take the system to the UC emission state. Similarly, photon avalanche (PA) upconversion uses one source for ESA from the metastable state, $|2\rangle$, while supporting energy transfers replenish the metastable state (see figure 2.4). The mechanism relies on cross relaxation events, also known as ion pair relaxation.

Cross relaxation is a type of energy transfer that occurs when an ion in a highly excited state transfers some (but not all) of its energy to a neighboring ground state ion. In the end, both ions occupy some intermediate state. Quite often, relaxation from these intermediate states are non-radiative and cross relaxation is classified as an undesirable quenching effect.

In PA upconversion, however, cross relaxation is desirable for the rapid promotion of ions to a metastable state as shown in figure 2.4. The scenario starts with one ion in the metastable state, which subsequently absorbs a photon and is promoted to a higher energy state, $|3\rangle$. Cross relaxation occurs with a neighboring ion, such that both ions are moved to the metastable state, $|2\rangle$.

Each of these can then repeat the loop and promote one more neighboring ion, leaving four ions in the metastable state. The pattern continues causing an avalanche of promotion events. The desired upconversion emission competes with this process in the following manner, introducing k_q as the cross relaxation rate coefficient

$$\frac{dn_1}{dt} = W_{31}n_3 + W_{21}n_2 - W_{12}n_1 - k_q n_1 n_3 \tag{2.10}$$

$$\frac{dn_2}{dt} = W_{12}n_1 + W_{32}n_3 - W_{23}n_2 - W_{21}n_2 + 2k_q n_1 n_3 \tag{2.11}$$

$$\frac{dn_3}{dt} = W_{23}n_2 - W_{31}n_3 - W_{32}n_3 - k_q n_1 n_3 \tag{2.12}$$

The solution to these equations defines two regimes, as in ESA and ET, where the proportionality between pump intensity and upconversion emission intensity differs. The threshold between the two regimes is called the pump threshold. It signifies the onset of a rapid increase in emission intensity vs pump power as is given by

$$W_{23}^{TH} = \frac{W_{21}(k_q + W_{32} + W_{31})}{k_q - W_{31}} \tag{2.13}$$

as determined previously by Joubert [18], Scheps [19], and Auzel [20]. The implications of this require $k_q > W_{31}$, and tells us that if $k_q >> W_{31}$, then $W_{23}^{TH} \approx W_{21} = \frac{1}{\tau_2}$. Therefore, the lower limit of the threshold is determined by the metastable level lifetime and a longer τ_2 gives a lower pump threshold. The definition of the rate coefficient, equation (2.4), implies that a large ESA cross section also provides a lower pump threshold.

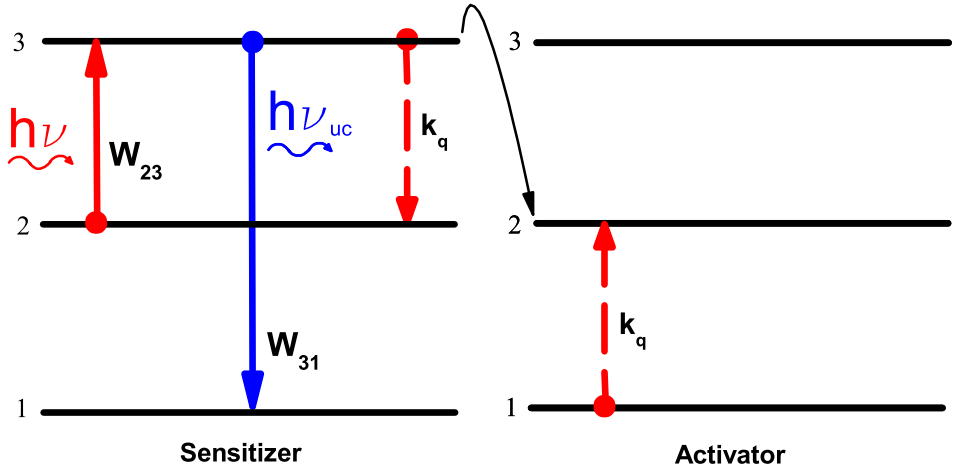

Figure 2.4: Energy level diagram depicting photon avalanche upconversion mechanism.

The rapid increase in emission intensity associated with the pump threshold can be observed in theory as a deviation from a linear slope in a log-log plot, as shown by Scheps [19] in figure 2.5. Below the threshold, some emission is observed due to the ESA process. This emission intensity is characterized by the excitation dependence discussed previously (equation (2.7)). Once cross relaxation events begin competing with radiative relaxation from the upconversion state, there is a rapid increase in emission as a function of pump power. Eventually, the emission reverts back to linear slope on the log-log plot as a reflection of its power dependence on the pump power.

Quite often, any given sample might exhibit properties of all three upconversion mechanisms. While the excited state absorption event is easier to understand and model, in general it requires two excitation sources. Meanwhile, the energy transfer and photon avalanche processes only require one excitation source. A carefully selected combination of dopant ions at higher concentrations than allowed for ESA often result in much higher luminescent output intensities for ET and PA upconversion.

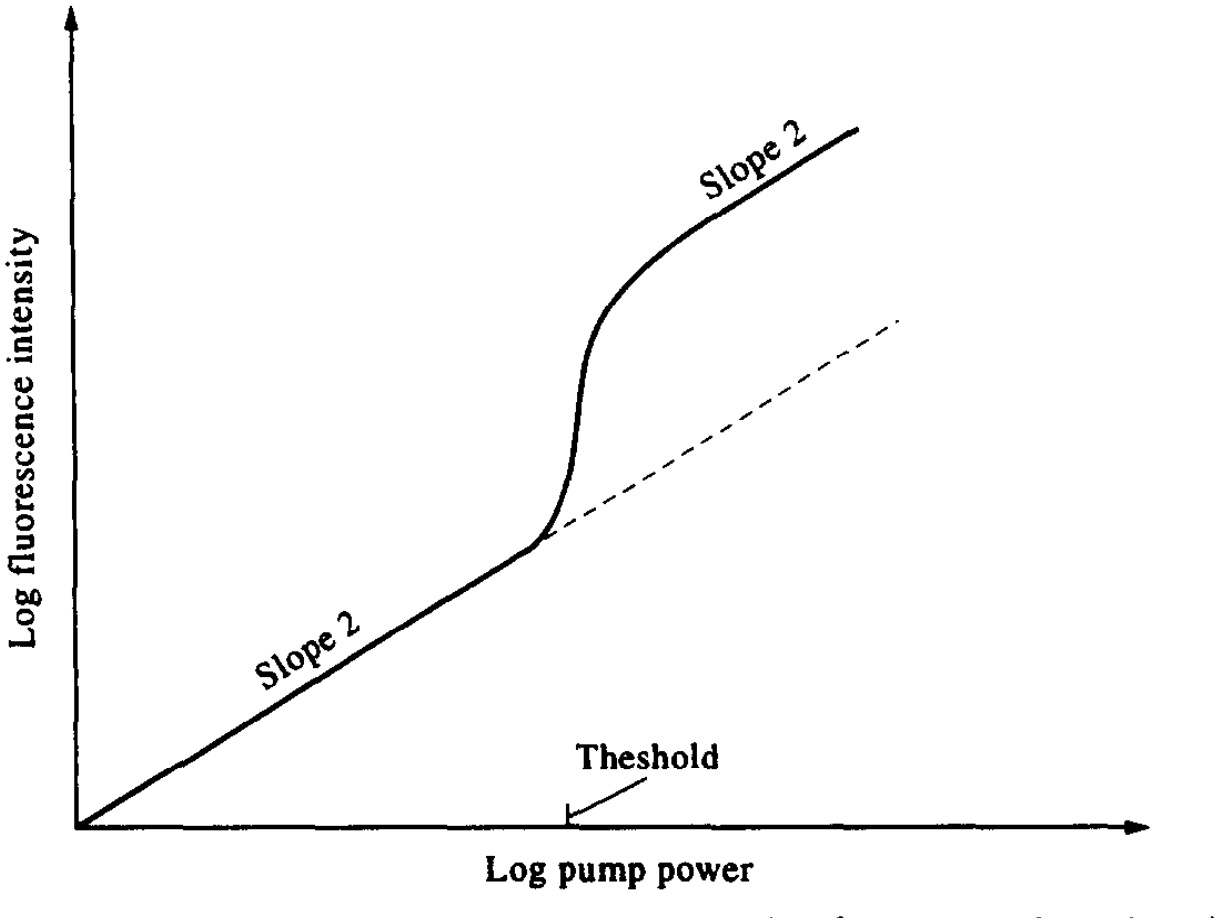

Figure 2.5: Plot of theoretical increase in upconversion emission intensity versus excitation pump power in the area neighboring the pump threshold. Graph obtained from Scheps [19].

Chapter 3

Background Review

Scientific research is built upon the discoveries of our colleagues and predecessors. As such, it is important to discuss a collection of works which contribute to the understanding of our particular combination of host and dopant ion. First, we will look at research related to the dopant, Er^{3+}. Then, we will consider works related to sulfide host materials. Finally, we will address the studies of CaS:Er^{3+}that have been published thus far.

3.1 Er^{3+}

Erbium was discovered in 1843 by Carl Gustaf Mosander of Ytterby, Sweden. Studies of erbium doped phosphors started as early as the 1960s and continue to gain interest today [34]. Because erbium is a rare earth element, its unfilled shell of twelve 4f electrons is shielded by three additional outer shells, 5s, 5p, and 6s* This shielding minimizes the effect of neighboring ligands such that the $^{2S+1}L_J$ states of erbium (and all other trivalent lanthanides) coincide well with the free ion energy levels, regardless of host. Due to this nature, the f-f transitions commonly observed in trivalent rare earth ions vary little from host to host. This behavior will help us establish some expectations for our own sample.

In 1963 Dieke and Crosswhite reported the now well known "Dieke" diagram, which maps the energy levels of trivalent rare earth ions based on absorption and fluorescence spectra of the ions in a lanthanum chloride ($LaCl_3$) host [35]. The observed and calculated levels for Er^{3+}, as presented by Dieke and Crosswhite, are shown in figure 3.1.

*In its common trivalent state, erbium loses the two electrons in the 6s shell and one of the twelve from the 4f shell.

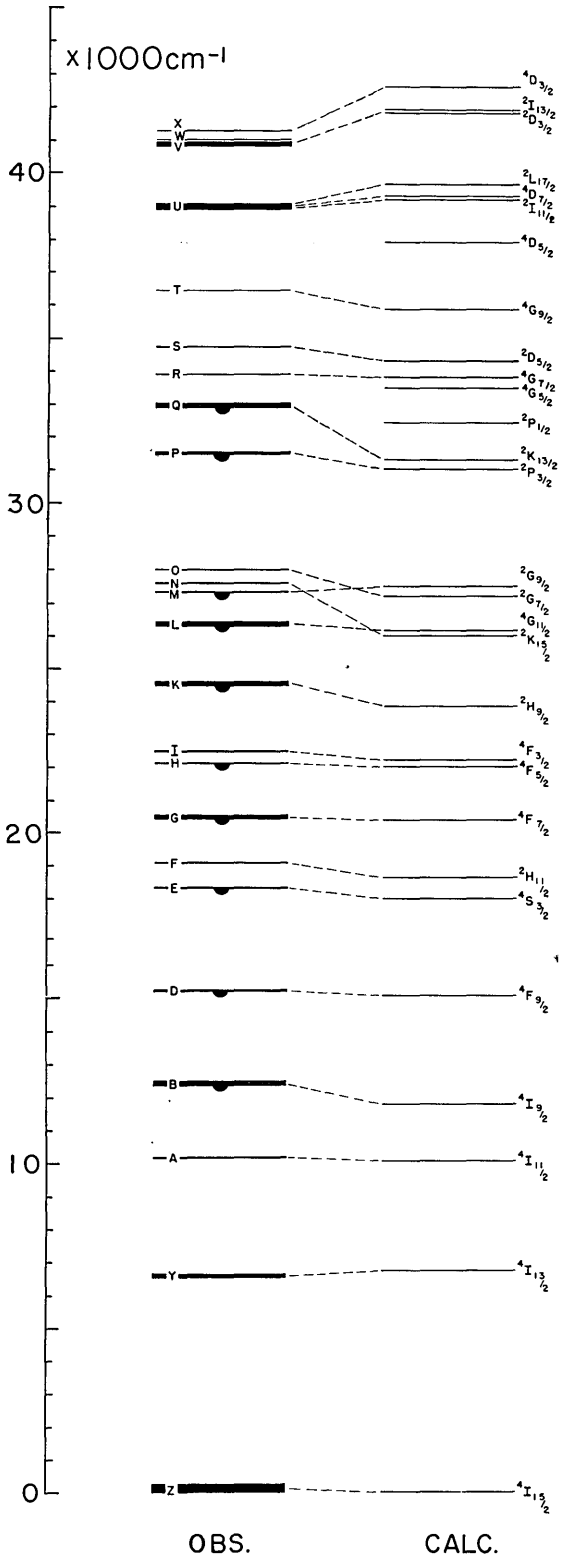

Figure 3.1: Observed and calculated levels of Er^{3+}as reported by Dieke and Crosswhite [35].

The number and spacing of energy levels in the Er^{3+}ion make it perfect for upconversion studies. Exciting the first excited state alone can result in as many as four subsequent excited state absorptions, $^4I_{15/2} \rightarrow ^4I_{13/2} \rightarrow ^4I_{9/2} \rightarrow ^4S_{3/2} \rightarrow ^2H_{9/2}$, converting 1.5 μm excitation into 410 nm emission (see figure 3.2(a)). If the Er^{3+}concentration is increased enough to foster energy transfers, as many as 35 different ETs must be considered for a complete understanding of the material [36]. The second and third excited states are also commonly used for the sequences $^4I_{15/2} \rightarrow ^4I_{11/2} \rightarrow ^4F_{7/2}$ and $^4I_{15/2} \rightarrow ^4I_{9/2} \rightarrow ^2H_{9/2}$ respectively (3.2 (b) and (c)).

Measured radiative lifetimes for the Er^{3+}energy levels can vary greatly for different hosts and different Er^{3+}concentrations within the same host. Different hosts exhibit different phonon frequencies which affect the potential for multiphonon relaxation. Table 3.1 shows measured lifetimes for 3 different hosts [36–38]. Some levels, for example $^4I_{9/2}$, are within range of the next lowest energy level to allow multiphonon relaxation so there is a difference by several orders of magnitude. Other levels, like $^4S_{3/2}$ or $^4I_{13/2}$, have a sufficient energy difference with respect to the next lowest level that multiphonon relaxation is not probable. Therefore the radiative lifetime varies little from host to host. But even these lone energy levels can be influenced by Er^{3+}concentration, as seen in table 3.2, which exemplifies a decrease in lifetime with increasing Er^{3+}concentration for a tellurite glass sample 3.2.

The increase in concentration corresponds to a decrease in ion proximity. Decreasing the distance between ions results in an increase in energy transfer events, like energy migration and upconversion, potentially decreasing the measured lifetime. By comparing our host system to other similar hosts, however, common characteristics emerge which we will discuss in the next section.

3.2 Sulfide hosts

While research on upconversion and infrared emission in CaS:Er has not been reported, two papers of similar systems should be examined. The first paper presents infrared luminescence

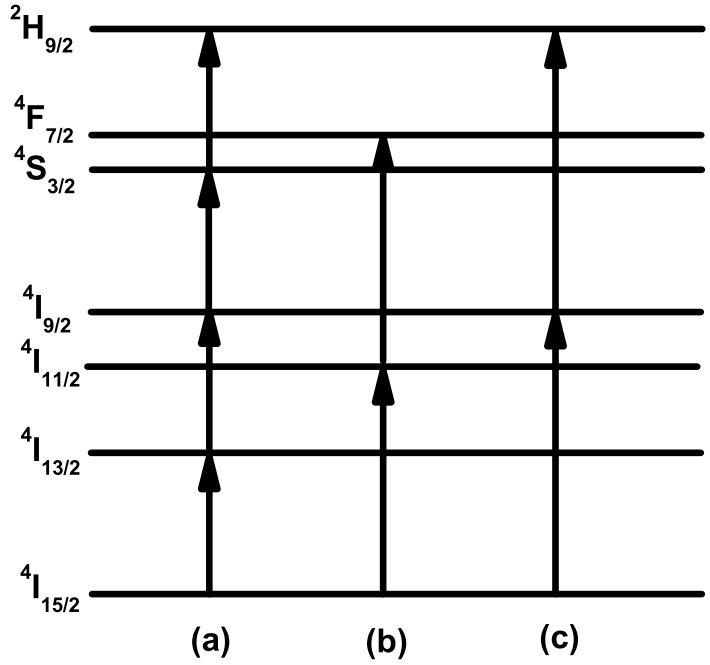

Figure 3.2: Three common ESA sequences for Er^{3+}doped materials. For clarity, the $^2H_{11/2}$, $^4F_{5/2}$, and $^4F_{3/2}$ energy levels are not included.

Table 3.1: Radiative lifetimes for the first five excited states of Er^{3+}in $Cs_3Lu_2Cl_9$, $LiYF_4$, and $60TeO_2$-20ZnO-$20ZnCl_2$-$ErCl_3$.

Material \ State	$^4I_{13/2}$	$^4I_{11/2}$	$^4I_{9/2}$	$^4F_{9/2}$	$^4S_{3/2}$	Ref
$Cs_3Lu_2Cl_9$:1%Er^{3+}	12.3 ms	7.1 ms	9.8 ms	171 μs	390 μs	[36]
$LiYF_4$:1%Er^{3+}	10 ms	2.9 ms	7 μs	55μs	400 μs	[37]
Tellurite glass	3.8 ms	3.1 ms	2.7 ms	350 μs	250 μs	[38]

due to Er^{3+}(2 at %) in a calcium thiogallate ($CaGa_2S_4$) host [39]. The second discusses upconversion in erbium doped sodium yttrium sulfide ($NaYS_2$)[9].

The calcium thiogallate work was reported in 2001 by Georgobiani *et. al.* for optical communication technologies [39]. While the 1.55 μm emission spectra were obtained by the direct excitation $^4I_{15/2} \rightarrow ^4I_{11/2}$, the decay curve relied on excitation at 337.1 nm via a ligand to metal charge transfer (LMCT), a broad absorption band at 300 nm where the host (ligand) sulfur atoms transfer energy to neighboring erbium atoms (metal) [40]. This method results in an observed lifetime of 2.7 ms for the $^4I_{13/2}$ energy level.

The work on $NaYS_2$ was presented in 2005 by Gerner and Güdel [9]. The study analyzed upconversion emission from laser excitation at a frequency of 10,000 cm^{-1}. Their research is mentioned because it shows efficient NIR to VIS upconversion in a low phonon energy sulfide host. The research also studies co-doped samples of $NaYS_2$:Yb^{3+}, Er^{3+}. Here the sulfide/Yb^{3+} LMCT band provides a quenching mechanism. The absorption edge of the band was found at a frequency of 23,000 cm^{-1}, whereas for $Er^{3+}$the absorption edge for the LMCT is at a frequency of 30,000 cm^{-1}. The lower energy onset of the LMCT band for Yb^{3+} makes it competitive with $^4S_{3/2}$ emission therefore quenching the green emission we are interested in.

3.3 Calcium sulfide doped with erbium

The first known study on erbium in a calcium sulfide host was done by Lehmann in 1971 [41]. His research studied calcium sulfide as a host for a total of 31 different activators. He also established that "purest CaS is not visibly luminescent," meaning any luminescence we observe can be attributed to the dopant itself and not the host material. Later studies have observed emission from pure CaS [42–44], but these signals can easily be distinguished from those originating from erbium.

The sample containing erbium was doped to a concentration of 1% and also included unreported amounts of phosphorus for the purposes of charge compensation. The data pre-

Table 3.2: Radiative lifetime of the first excited state in $60TeO_2$-$20ZnO$-$20ZnCl_2$-x$ErCl_3$ for x = 0.1, 1, 3, 5, and 10 mol%.[38]

$ErCl_3$ (mol%)	$^4I_{13/2}$ τ_R
0.1	4.2 ms
1	3.7 ms
3	3.4 ms
5	3.1 ms
10	2.2 ms

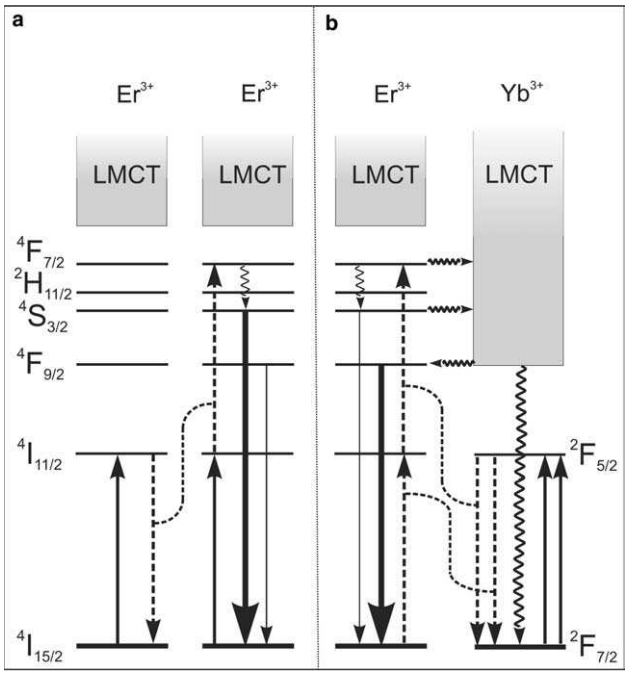

Figure 3.3: The effects of $Er^{3+}$and Yb^{3+} LMCT bands on upconversion processes in $NaYS_2$. Image obtained from Gerner and Güdel [9].

sented by Lehmann reports an emission and absorption spectra over the range of 2.0 to 5.0 eV (see Figure 3.4). No data regarding IR emission or upconversion was presented.

Several other studies have been reported since then, focusing on UV and VIS excitation, electroluminescence, and even phosphorescence. At this point, however, no reports of upconversion or measurements of IR transitions have been published.

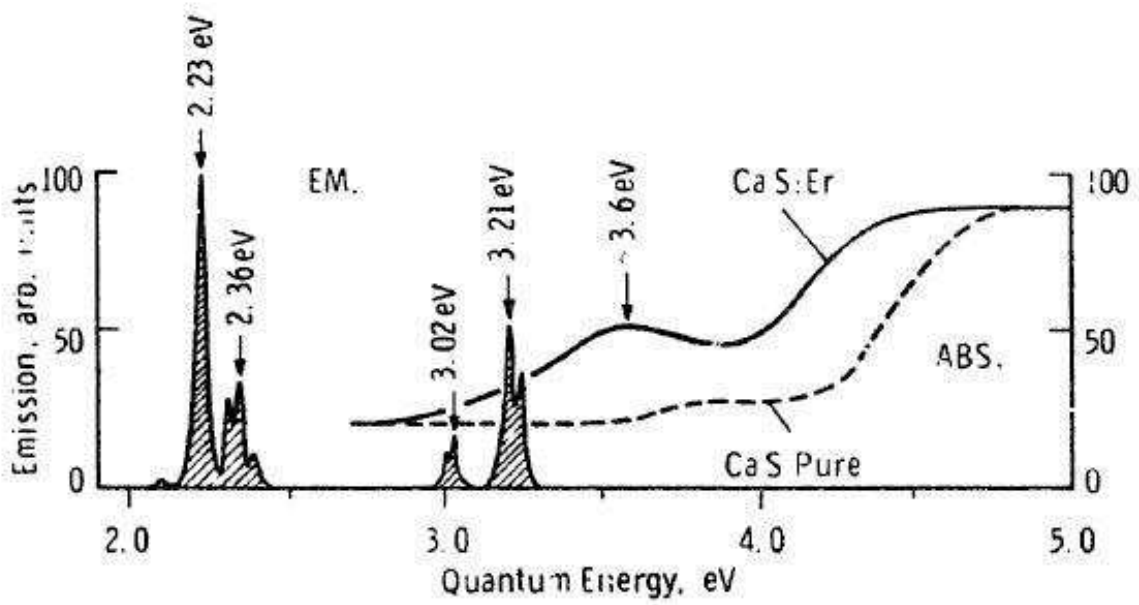

Figure 3.4: Emission and absorption spectra of CaS:Er^{3+}(1%), P. Graph obtained from Lehmann [41].

Chapter 4

CaS:Er^{3+} Fabrication and Confirmation

4.1 Fabrication Method

Fabrication of the erbium doped calcium sulfide was based on a method used by Okamoto [45] for cesium doped calcium sulfide phosphors. The Okamoto method benefits from its single step reaction, as opposed to other similar methods which require a two-step reaction [46, 47].

$$CaCO_3 + Ce_2(SO_4)_3 \cdot 8H_2O + Na_2CO_3 + S \xrightarrow[1-72\ hours]{800-1100\,^{\circ}\mathrm{C}} CaS:Ce^{3+} \tag{4.1}$$

The modified method requires the use of the following raw materials: calcium carbonate ($CaCO_3$), sodium carbonate (Na_2CO_3), sulfur (S), and erbium sulfate ($Er_2(SO_4)_3 \cdot H_2O$). The materials used were all in powder form and of at least A.C.S. reagent quality. The calcium carbonate and sulfur were acquired from J. T. Baker and the sodium carbonate from Fisher Scientific. The erbium sulfate was a 99.9% pure powder obtained from Alfa Aesar. The components were mixed by mortar and pestle in a molar ratio of 4:1:1 for S:$CaCO_3$:Na_2CO_3. Enough erbium sulfate was added to result in a 0.1% doping level (based on relative molar quantities). This ratio provides an excess of sulfur, which acts as a flux during the heating process.

The mixed raw materials are placed in a covered 30 mL alumina crucible which is placed inside a 50 mL alumina crucible and surrounded by a layer of carbon powder. The carbon reacts readily with any oxygen present during the heating process and prevents the formation of calcium sulfate ($CaSO_4$), an undesirable byproduct. The larger crucible is also covered

and placed inside a small furnace (Thermolyne Type 48000). Bulk Na_2CO_3 does not reach its melting point until 851 °C, so the procedure calls for temperatures from 800 °C to 1100 °C for as long as 72 hours. The melting point of sulfur occurs between 110 °C and 119 °C. Its boiling point is reached at 444 °C, however, under explosive conditions sulfur may auto-ignite anywhere from 248 °C to 266 °C. When heated, sulfur may decompose into sulfur dioxide (SO_2) gas and hydrogen sulfide (H_2S), both of which are toxic and should not be inhaled. For these two reasons (flammability and toxicity) the furnace should be kept within a fume hood throughout the heating process. The material for this research was heated at 1030 °C for 40 hours. After slowly cooling to room temperature, the inner contents were solid, porous, and off-white in color.

A subsequent filtration was needed to remove unreacted materials and flux products. The chosen flux and its byproducts are extremely hygroscopic and therefore easily removed through a water (suction) filtration step. Since CaS is also known to be hygroscopic (but to a lesser degree than the flux and other byproducts) [48], filtration required the use of cold doubly distilled water and cold* ethanol (USP grade, Aaper Alcohol and Chemical Company). The cold water was added to the solid product in the smaller crucible and was mixed with a scraper until the water turned cloudy. The cloudy cold water was then poured onto a Bükner funnel with medium porosity filter paper (Whatman Grade No. 1, 11 μm particle retention), connected to a side-arm flask which was evacuated by a small mechanical pump. The filtered contents were then rinsed with the cold ethanol. This process was repeated until the majority of the crucible's contents were removed. At this point, the filtered product had the appearance of small grains of sand. The grains were rinsed one final time with cold ethanol and placed in a test tube.

For the drying process a small clam shell furnace (Hevi-Duty Electric Company) was used to heat the sample. Still within the test tube, the sample was placed inside a larger quartz tube (16 inches long with a 1 inch outer diameter) along with a thermocouple (K

*Both the distilled water and ethanol were stored in a refrigerator maintained at 6 ° C.

type, Omega XC-24-K-12). The temperature of the tube's interior was kept at 100 °C for one hour and the quartz tube was evacuated by a mechanical pump during the heating process to remove any remaining moisture. The drying temperature was regulated by an Omega CNi1622C24 temperature controller, connected to an Omega SSR330AC25 solid state relay which cycled power to the furnace. After drying, the sample was removed from the test tube and stored in a small plastic bottle inside a desiccator.

4.2 XRD Confirmation

Confirmation of the product was obtained by x-ray diffraction (XRD), using a Scintag Pad V x-ray diffractometer. The sample grains were finely ground with a mortar and pestle, suspended into cold ethanol, and applied to a frosted quartz glass slide via a dropper. Once the ethanol evaporated, the slide was placed within the x-ray beam path and the detection angle of the beam was scanned from 10 ° to 70 °, with a step size of 0.05 °. The X-ray emitter was operated at a voltage of 40 kV and a current of 40 mA.

The detection angles are related to atomic spacings through the use of the Bragg equation,

$$n\lambda = 2d \sin\theta \tag{4.2}$$

Given that the Pad V operates with a copper x-ray emitter, which emits at 1.5418 Å, determining the atomic spacing "d" from the detection angle 2θ is easily done. The three peaks in figure 4.1 have been labeled accordingly. The three largest known peaks for calcium sulfide are represented in figure 4.1(b) at 2.846 Å, 2.013 Å, and 1.644 Å. These three peaks correspond to diffraction from the (200), (220), and (222) planes of the calcium sulfide crystal structure as shown in figure 4.2. Excellent correlation between the known peaks and the data from our sample confirms that the powder contains calcium sulfide and no other sizable defects.

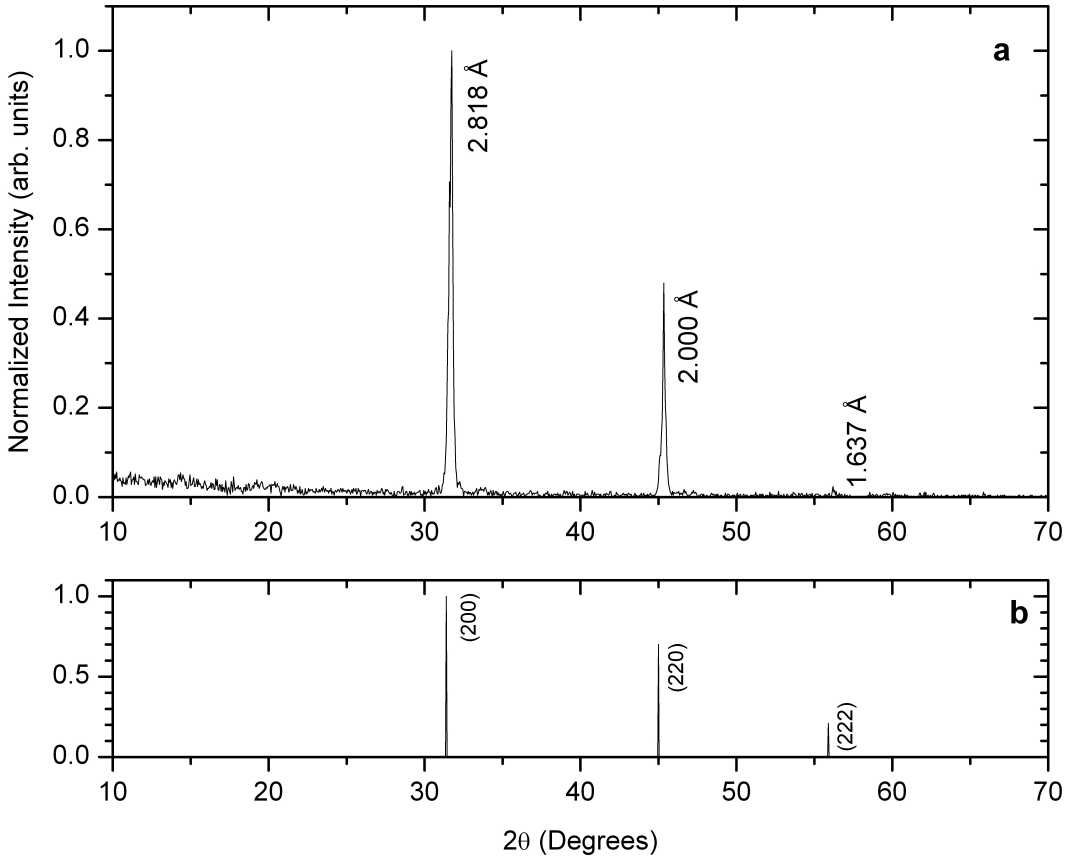

Figure 4.1: X-ray diffraction data for CaS:Er 0.1%. (a) Normalized counts as a function of scanning angle 2θ. Peaks are identified by their calculated value for "d", in units of Angstroms. (b) Normalized relative counts for the three most prominent known peaks for CaS powder.

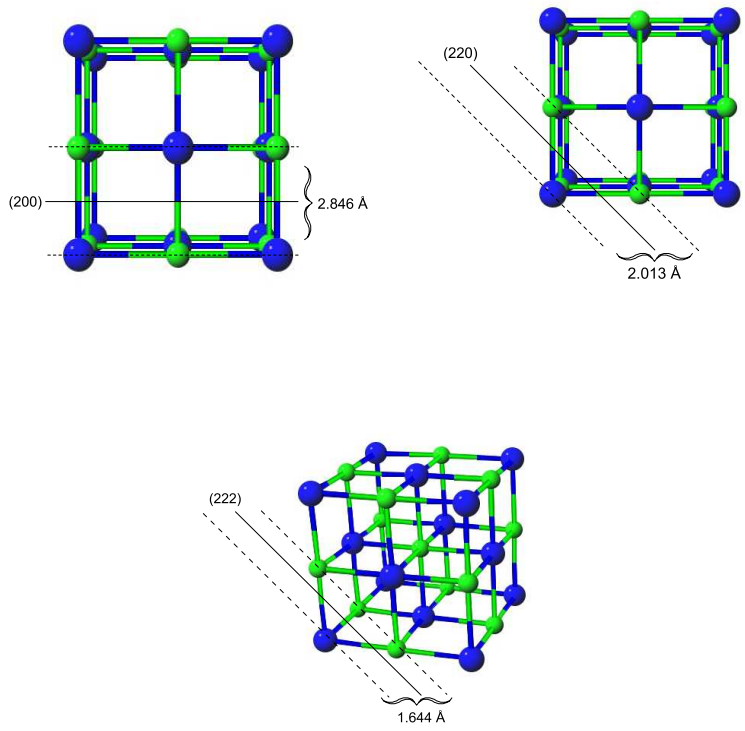

Figure 4.2: Crystal structure of calcium sulfide, indicating the (200), (220), and (222) planes. Structure images obtained from the Crystal Lattice Structures Web page [49].

The resulting material exhibited the expected properties of an erbium upconverting phosphor (VIS luminescence from NIR photoexcitation), but these properties are relevant regardless of the choice of host lattice (see page 16). Concern about whether the erbium was incorporated into the CaS lattice or present in connection with a trace defect, like $CaSO_4$, was soon dispelled by the following experiment.

Taking advantage of the hygroscopic nature of CaS, we allowed the material to deteriorate into its oxidized form, $CaSO_4$. If the erbium ions were incorporated into the host CaS lattice, then VIS emission would diminish once the host oxidizes. If the erbium ions were initially connected to trace $CaSO_4$, then the conversion of CaS to $CaSO_4$ would not diminish the material's VIS emission.

The oxidation technique used was published in 1997 by K. Qui et al and involves heating the sample in moist air for one hour [50]. Heating in this manner, at 865 °C is reported to cause a 48.67% conversion of CaS to $CaSO_4$. A diagram (4.3)representing the setup used for our erbium doped sample lists the equipment used for the procedure, most of which has been discussed already (see drying procedure on page 25). Atmospheric air (21% O_2 by volume) is compressed to 30 psi and pumped through a nylon tube to a rotameter which reduces the air flow by 50%. The controlled flow of dry air is bubbled through a sealed erlinmyer flask and sent into a quartz tube via an ultra high vacuum T-junction. The other side of the T-junction allows entry of the K-type thermocouple. The quartz tube that contains the thermocouple also holds a small quartz boat for the powder sample. The opposite end of the quartz tube connects to copper tubing immersed in a one liter beaker filled with water. This step cools the emerging hot gas. The cooled gas travels through a bubble counter filled with diffusion pump oil, used to maintain a positive pressure and steady exhaust. Finally, the gas is carried safely out of the building by a plastic tube.

After oxidation, the sample material was compared to a control sample stored in the desiccator. XRD analysis showed no change in the molecular contents of the control. The scan for the oxidized sample, however, contained four strong peaks that correspond to the

four strongest peaks known for powder $CaSO_4$ (see figure 4.4). The VIS emission from the two samples revealed no upconversion properties in the oxidized sample, but maintained VIS luminescence in the control, thus confirming erbium integration into the CaS host lattice. The next chapter will give details for the photoluminescence and other optical experiments performed to better understand the nature of this material.

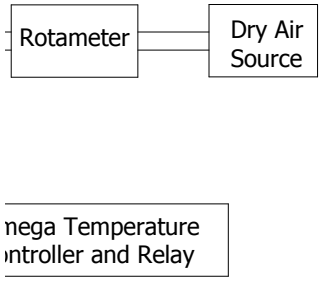

Figure 4.3: Schematic diagram of the heating assembly for the oxidation of CaS:Er^{3+}.

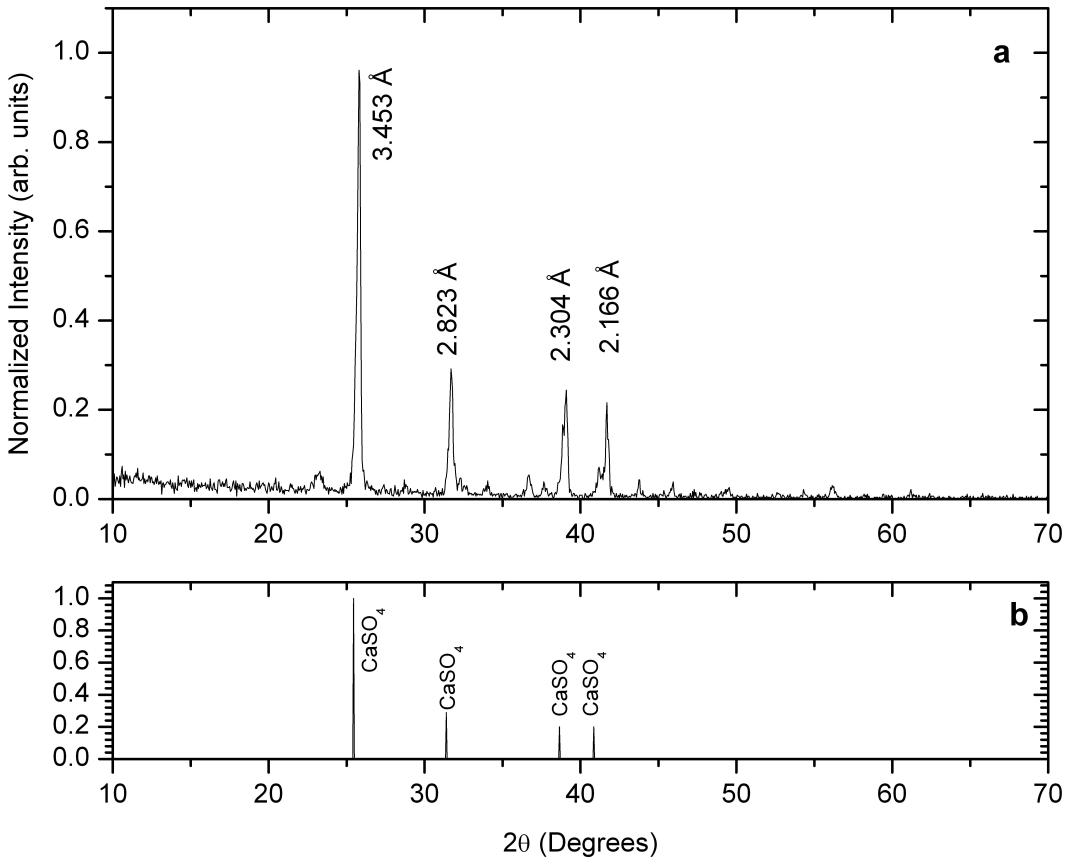

Figure 4.4: X-ray diffraction data for CaS:Er 0.1% after oxidation at 865 °C for one hour. (a) Normalized counts as a function of scanning angle 2θ. Peaks are identified by their calculated value for "d", in units of Angstroms. (b) Normalized relative counts for the four most prominent known peaks for $CaSO_4$ powder.

Chapter 5

Upconversion Studies

In order for the CaS:Er^{3+}(0.1%) phosphor to be a realistic solution for medical applications, three qualities must be present. First, photoluminescent emission as a result of upconversion must lie in a useful window of the VIS range. Many upconverting phosphors containing erbium emit well into the UV range as a result of 3 and 4 photon UC processes [51]. At 400 nm and shorter, endogenous cellular components, like DNA and native porphyrins, begin to absorb and are damaged [52]. Therefore, materials that emit in the UV must be avoided for *in vivo* applications. At wavelengths longer than 700 nm the human tissue absorption diminishes, rendering the need for an internal upconverter useless. Hence, the useful window for PL emission lies between 400 nm and 700 nm.

Second, the excitation source used for both GSA and ESA must occur in a specific wavelength region where human tissue absorption is minimal. At the low wavelength limit, onset of VIS absorption due to blood cells occurs as low as 650 nm for oxygenated hemoglobin and as high as 780 nm for deoxygenated hemoglobin [53]. At the other end of the spectral range water begins absorbing in the NIR at wavelengths as short as 910 nm. The absorption coefficient (absorption factor) as a function of wavelength is shown in figure 5.1 for the three materials.

The relationship between the incident intensity of light and the transmitted intensity is known as Lambert's law [54]

$$I(\nu) = I_0(\nu)e^{-\alpha(\nu)d} \tag{5.1}$$

and is used here to determine α by comparing I and I_0 for a given thickness, d, according to the following

$$\alpha = \frac{1}{d} \ln \frac{I_0}{I} \tag{5.2}$$

The minimum absorption wavelength occurs at 800 nm, but an excitation wavelength anywhere between 700 nm and 900 nm would be acceptable.

Finally, the upconversion process must be efficient enough to be considered viable. Once we know the energy efficiency of the system we can determine what amount of NIR radiation the target tissue must receive before a noticeable response is expected. Each of these three criteria are essential for proof of concept and must be addressed.

5.1 Spectroscopic Methods

In all measurements (except efficiency testing), a small amount of sample material in its powder form is packed inside a custom built aluminum sample holder and held in place behind a quartz window. Low temperature (77 Kelvin) measurements are acquired with the use of an Oxford Optistat Bath Cryostat filled with liquid nitrogen. Sample temperature is stabilized by an Oxford ITC601 temperature controller and a sample space heat exchanger. All post collection data analysis is performed using the Origin Data Analysis and Graphing software (OriginLab Co.).

5.1.1 Photoluminescence

A photoluminescence (PL) study provides information about the relative intensity of light emitted by a sample as a function of wavelength, for a specific excitation wavelength. Most photoluminescence studies involve irradiating the sample with a shorter wavelength, higher frequency source than the observed emission. As we are interested in photoluminescence from upconversion, we require an excitation source in the NIR; i.e. at a lower frequency than the observed emission range. The continuous wave (CW) Ti-Sapphire laser (Spectra Physics, 3900S) is capable of lasing within the excitation range of interest (700 nm to 900 nm) and

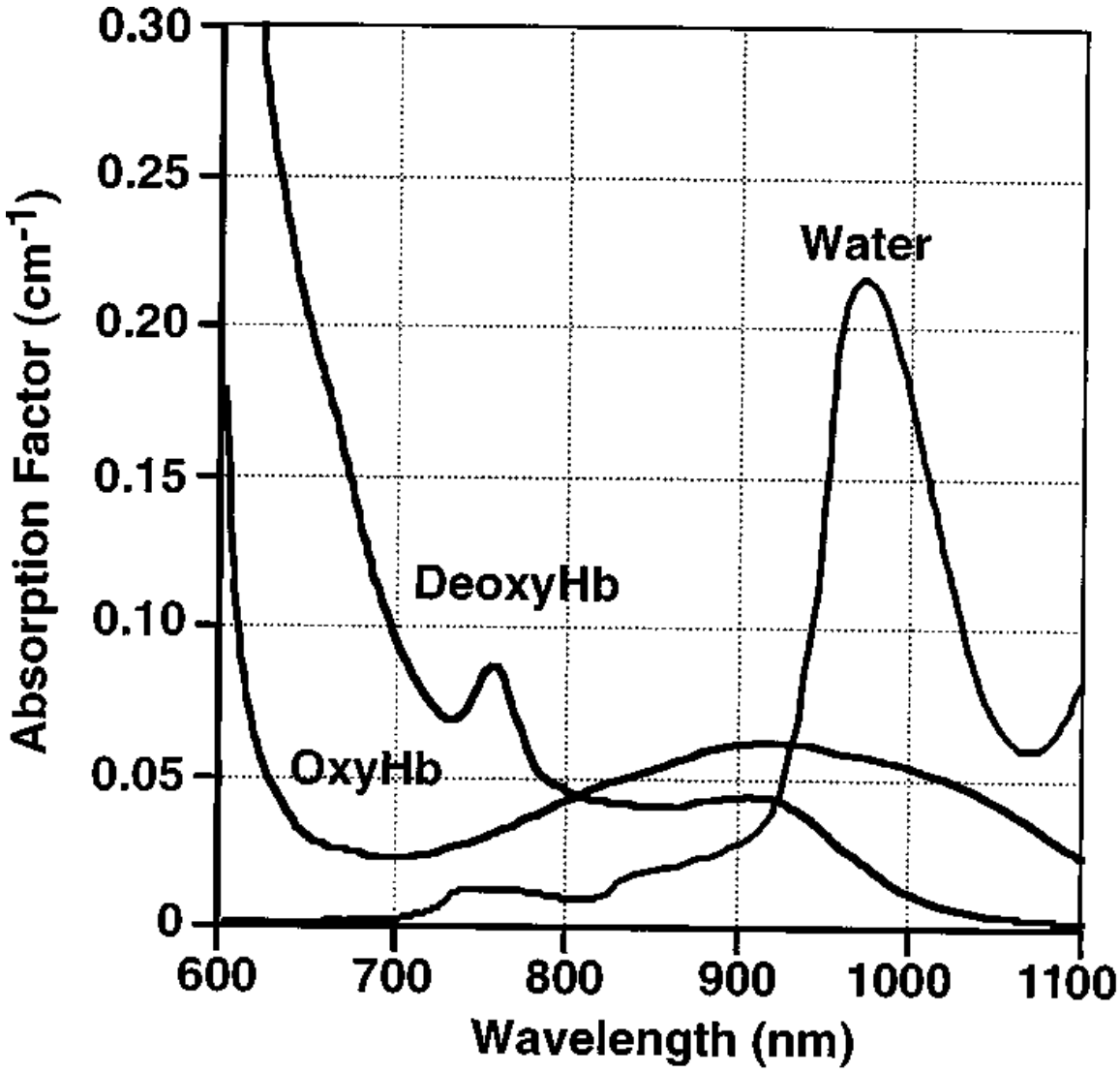

Figure 5.1: Optical attenuation [$\log_{10}$] for 1 cm depth of deoxygenated hemoglobin, oxygenated hemoglobin, and water. Hemoglobin concentration equals 210 μM in water. Image obtained from [53].

provides a narrow linewidth (<40 GHz), high power (2.5 W maximum) beam when pumped by an argon ion laser (Spectra Physics, Stabilite 2017). The output frequency can be tuned using an intracavity birefringent filter.

For the purpose of this study, the Ti-Sapphire laser is tuned to a wavelength of 803.5 nm and focused onto the sample at room temperature at an angle of 45°with respect to the sample surface normal. The sample surface faces a lens (1" diameter, 50.2 mm focal length) which collects the emitted light onto a UV grade fiber optic cable. Before reaching the cable, the NIR portion of the collected light is attenuated by a 1.0 mm thick Schott glass filter (BG-39). The fiber optic cable leads to a single monochromator (Acton, SpectraPro 275) through a 5.0 μm entrance slit. Within the monochromator, the collected light is dispersed by a reflection grating (150 grooves/mm, 300 nm blaze) onto a nitrogen cooled UV/VIS capable charge coupled device or CCD (Princeton Instruments, LN/CCD512TKB UV). Data is collected by a software package based on the LabView work environment custom built by the Happek research group.

5.1.2 Photoexcitation

While PL analyzes emission as a function of wavelength at a given excitation frequency, photoexcitation analyzes a range of excitation frequencies for a given emission wavelength. The result is a collection of relative emission intensities as a function of excitation frequency. Taking advantage of the scanning range of the Ti-Sapphire laser, low temperature (77 K) photoexcitation data is recorded using an experimental setup similar to the photoluminescence measurements. After excitation by the Ti-Sapphire laser, the light emitted by the sample is filtered by a 1.0 mm thick Schott glass filter (BG-39) and focused onto a fiber optic cable. The collected signal is passed through the 1.0 μm entrance slit of a SpectraPro 275 monochromator, dispersed with a reflection grating (50 grooves/mm, 600 nm blaze), and recorded by a VIS light sensitive CCD (SBIG ST-6 Optohead), thermoelectrically cooled to -20°C. Data is collected using KestrelSpec software (Catalina Scientific).

Adjusting the dichroic filter of the Ti-Sapphire laser by means of a micrometer screw allows data to be recorded at different excitation wavelengths. As the excitation wavelength was increased by intervals of 0.25 nm over a range of 780 nm to 824 nm, an emission spectrum was recorded over the range of 425 nm to 735 nm for each step. Each spectrum was integrated over the range corresponding to green emission range from the sample and a plot of the integrated emission as a function of excitation wavelength was compiled.

5.1.3 Pump Intensity Dependence of Upconversion Emission

Discovering the influence of excitation pump intensity on photoluminescent emission intensity also requires an experimental setup similar to the photoluminescent measurements. Instead of recording just one emission spectrum, however, multiple emission spectra are recorded while adjusting the excitation power. This adjustment is made through the use of a continuously variable neutral density filter wheel. As the wheel is rotated, a continuous reduction in optical transmittance, from 100% down to 25%, can be observed over a full 360°rotation.

Each manual movement of the wheel is accompanied by a power reading of the laser and an emission spectrum. Power readings are recorded by a Spectra Physics 407A power meter. The excitation beam cross section was measured by gradual eclipsing with a sharp knife-edge [55].

Photoluminescent emission is collected by a 2" focal length (2" diameter) lens, passed through a 1.0 mm thick Schott glass filter (BG-39), onto a UV grade fiber optic cable. From here, signal processing and data collection proceeds just as it did for the photoluminescence measurements. The emission spectra were integrated over specific wavelength ranges corresponding to known optical transitions and plotted as a function of incident pump intensity.

5.1.4 Energy Efficiency Measurements

Energy efficiency (η) is defined by the total useful energy output of a system divided by the total energy put into that system. For a linear optical transition, this can be measured

by the total photoluminescent output intensity (I_{pl}) divided by the total photoexcitation intensity (I_{exc}). In the case of upconversion, a nonlinear optical transition, the output intensity increases by a power of n as the excitation intensity increases, for an n photon process. In other words, different pump intensities will result in different energy efficiency ratings. To standardize efficiency measurements, the results should be normalized by the excitation intensity as defined by the following,

$$\eta = \frac{I_{pl}}{I_{exc}^{n}} \tag{5.3}$$

In the case of a two photon UC process, $n = 2$ and therefore η simplifies to

$$\eta = \frac{I_{pl}}{I_{exc}^{2}} \tag{5.4}$$

Note that while η is normally a unitless quantity, the general normalization rule requires η to have units of $(cm^2/W)^{n-1}$.

The photoluminescent intensity measurement requires the use of an integrating sphere. The sphere uniformly scatters the sample's emitted luminescence such that the total emission can be inferred from the emission detected within any finite area (usually the size of the detector).

To achieve this measurement, the throughput for green light in the sphere is calculated by comparing the incident intensity of a green (532 nm) diode pumped Nd:YAG laser (B & W Tek) to the detected intensity at the side port (see figure 5.2). Once the system throughput is known, we can calculate the total luminescent intensity of our phosphor from the detected output divided by the sample cross section. The excitation power is measured directly with the Spectra Physics 407A power meter and divided by the sample cross section to obtain the excitation intensity I_{exc}. The incident excitation beam was expanded to a diameter of 1/4" to reduce the effects of a spatially varying intensity illuminating the sample area (1/8"

diameter). The scattered excitation signal was attenuated by the previously mentioned BG-39 filter and the remaining NIR signal was isolated and accounted for by a 3.0 mm thick Schott glass filter (RG715).

5.2 Results

Room temperature measurements of photoluminescent emission are shown in figure 5.3. Ground state relaxations from most of the energy levels in the frequency range from 16000 cm^{-1} to 29000 cm^{-1} are present. The highest frequency emission observed corresponds to a transition from $^2H_{9/2}$ to the ground state, as shown in pathway (a) of figure 5.4. The second excitation pathway, (b), involves multiphonon relaxation of the $^4I_{9/2}$ state (populated by GSA) to the $^4I_{11/2}$ level. Subsequent ESA from $^4I_{11/2}$ excites the ion into the $^4F_{3/2}$ state. States $^4F_{3/2}$ and $^4F_{5/2}$ are in close proximity and often treated as one combined level. In this case,$^4F_{3/2}$ relaxes non-radiatively and emission is seen as a result of ground state relaxation from $^4F_{5/2}$.

Alternatively, non-radiative relaxation from $^4F_{3/2}$ branches to the $^4F_{7/2}$, $^2H_{11/2}$, and $^4S_{3/2}$ states, resulting in the three peaks observed at frequencies 20150 cm^{-1}, 18800 cm^{-1}, and 18050 cm^{-1} respectively. The $^4S_{3/2}$ and $^2H_{11/2}$ states are also in close proximity to each other, acting as one combined level in thermal equilibrium at room temperature. Here we see distinct peaks corresponding to each transition, but at low temperatures, thermal excitation of the $^2H_{11/2}$ state ceases and emission at 18800 cm^{-1} diminishes (see figure 5.5).

Supporting evidence for the nature of the two pathways comes from the measurements of pump intensity dependence on upconversion emission from the $^2H_{9/2}$ and the $^4S_{3/2}$ relaxations at 24400 cm^{-1} and 18050 cm^{-1} respectively. The low intensity approximation, derived on page 6, states that for a two photon process a linear increase in excitation intensity results in a quadratic increase in UC photoluminescent intensity. In general, an n photon process results in a relationship given by $I_{pl} \propto I_{exc}^n$. The predicted pathways will result in an I_{exc}^2

dependence which, if plotted on a log-log scale of excitation intensity versus PL intensity, would correspond to a straight line with a slope equal to 2.

At low pump intensities (below 1 W/cm^2), the slopes for the $^2H_{9/2}$ transition and the $^4S_{3/2}$ transition approach 1.9. This P^2 dependence confirms that the two photoluminescent peaks are the consequence of two photon processes and no three photon processes have been detected.

Low temperature photoexcitation results reveal that the most intense green photoluminescence occurs when the sample is excited at 803.5 nm 5.8. At 77 Kelvin only three of the eight total stark levels within the ground state multiplet are thermally accessible, as indicated by the triplet pattern seen at frequencies 12315 cm^{-1}, 12422 cm^{-1}, and 12563 cm^{-1}. The overall structure is a superposition of the strongest peaks of the $^4I_{15/2} \rightarrow ^4I_{9/2}$ transition with the strongest peaks of the $^4I_{11/2} \rightarrow ^4F_{3/2}$ transition. All of the peaks are well within the range desired for medical technologies, between 700 nm and 900 nm (14300 cm^{-1} and 11100 cm^{-1}), and are close to the optimum wavelength of 800 nm (12500 cm^{-1}).

So far the results indicate that CaS:Er^{3+}could serve a promising role for future medical technologies. The only condition to be determined is the energy efficiency of the red-to-green upconversion. Unfortunately, the efficiency was found to equal 9.97×10^{-7} cm^2/W*, a factor of ten smaller than average ESA materials [20]. To give an idea of how this relates to the total PL intensity, imagine exciting with a 1 W beam, focused to a spot size of 1 mm (A=π(0.05 cm)^2 = 0.008 cm^2).

$$I_{pl} = \eta \cdot I_{exc}^2 = \eta \frac{P_{exc}^2}{A^2} \approx 1 \times 10^{-6} \frac{cm^2}{W} \frac{(1\ W)^2}{(0.008\ cm^2)^2} = 0.016\ W/cm^2 \tag{5.5}$$

Within human tissue, different cellular components absorb and scatter light in different ways. This information can be used to distinguish between different types of tissue, even those containing malignant and benign cells [56, 57]. As a general rule, however, the mean free path or average distance between scattering events is 1 mm [53].

*Units reflect normalization required for comparative efficiency calculations.

At 800 nm, the penetration depth for human tissue (based on *in vivo* studies of the human hand) is 3.0 mm[58]. This means a focused beam traveling through 15 cm of tissue is attenuated by a factor of $(1/e)^{50}$ or approximately 2×10^{-22}. A large excitation area, however, would minimize the effects of scattering and reduce the attenuation to the following,

$$I/I_0 = e^{-\alpha d} \tag{5.6}$$

With an average value of $\alpha = 0.1$ cm^{-1}, a tissue depth of 15 cm causes an attenuation of $(1/e)^{3/2}$.

Current clinical trials using 800 nm diode lasers for various medical treatments show permanent tissue damage at intensities above 500 W/cm^2 [59], but at 10 W/cm^2 (1800 J/cm^2 for a 3 minute exposure) no permanent damage is observed [60]. Both tests did require some form of cooling at the surface epidermal layer to minimize patient discomfort.

This level of excitation, after traveling through 15 cm of tissue, would reduce to 2.23 W/cm^2. Note that multiple scattering events will increase the mean path length and therefore attenuation due to absorption should be increased even further. We can account for this by further reducing the excitation intensity to 1 W/cm^2 (an optimistic approximation). If we apply the measured energy efficiency, η, we can determine the PL intensity per ion.

$$\mathrm{I_{pl}} = \eta \mathrm{I_{exc}^2} \approx 1\times10^{-6}\frac{\mathrm{cm^2}}{\mathrm{W}}\left(1\frac{\mathrm{W}}{\mathrm{cm^2}}\right)^2 = 1\times10^{-6}\ \mathrm{W/cm^2} \tag{5.7}$$

Therefore, a 1 μm particle with a surface area of 3×10^{-12} cm^2 will emit a total PL output power of 3×10^{-18} W or total energy output of 3×10^{-13} J for a one second exposure. Since the energy of one 555 nm photon is equal to 3.58×10^{-19} J, we can estimate approximately 10 photons a second. Several factors may require this number to be reduced even further (smaller phosphor size, lower initial intensity, larger tissue depth, larger absorption coefficient).

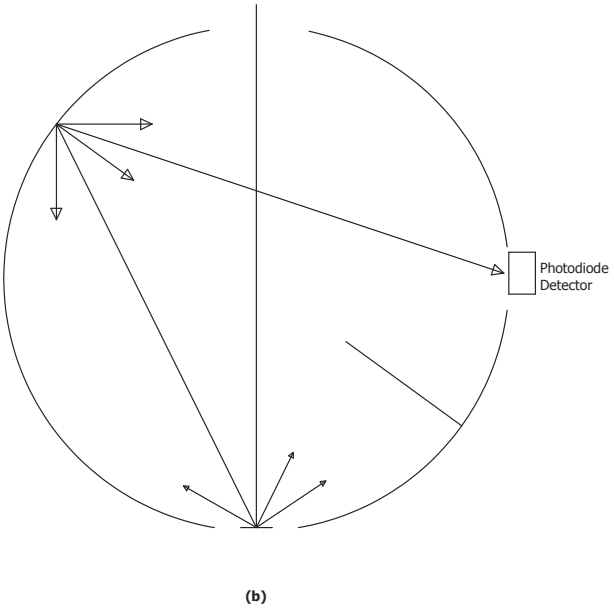

Figure 5.2: Integrating sphere schematic. (a) Incident radiation enters from the top port and excitation power is measured after passing through a 1/8" diameter aperture at the bottom of the sphere. (b) Phosphor held in a cup with diameter equal to 1/8" is excited. Diffuse emission is measured by a photodiode from the side port.

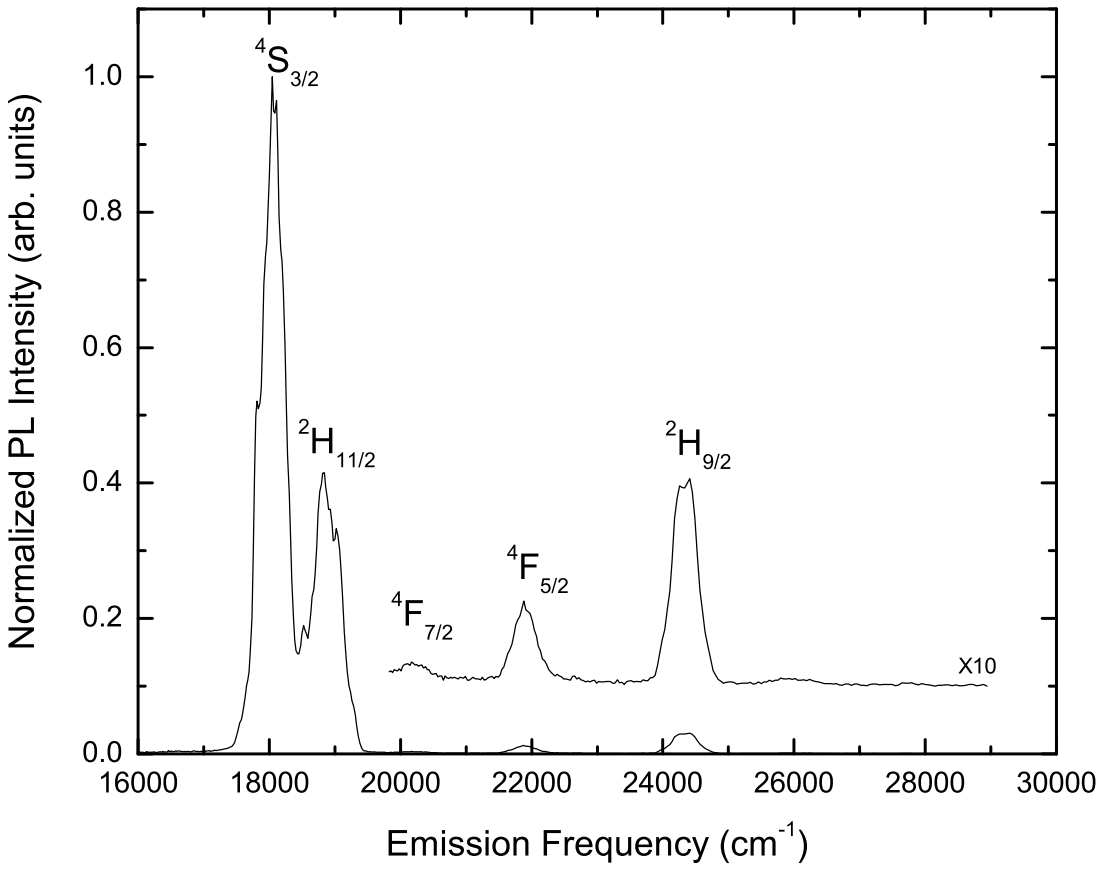

Figure 5.3: Photoluminescent spectrum of CaS:Er^{3+}(0.1%) at room temperature by 803.5 nm excitation. Peaks are due to ground state relaxation from the indicated excited state.

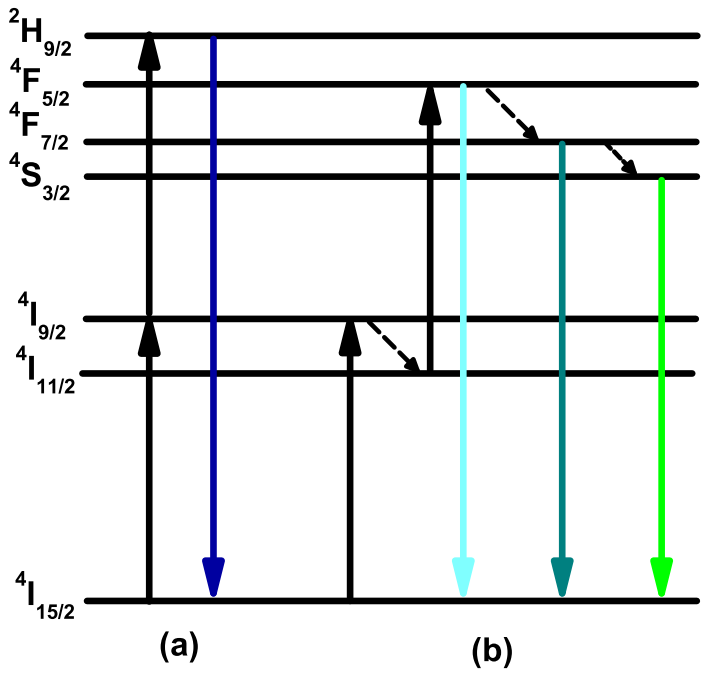

Figure 5.4: ESA pathways of CaS:Er^{3+}(0.1%) as a result of 803.5 nm excitation. Solid black lines indicte excitation, dashed lines show non-radiative relaxation, and colored lines represent ground state relaxation from excited states. For clarity, the $^4I_{13/2}$, $^2H_{11/2}$, and $^4F_{3/2}$ levels are omitted.

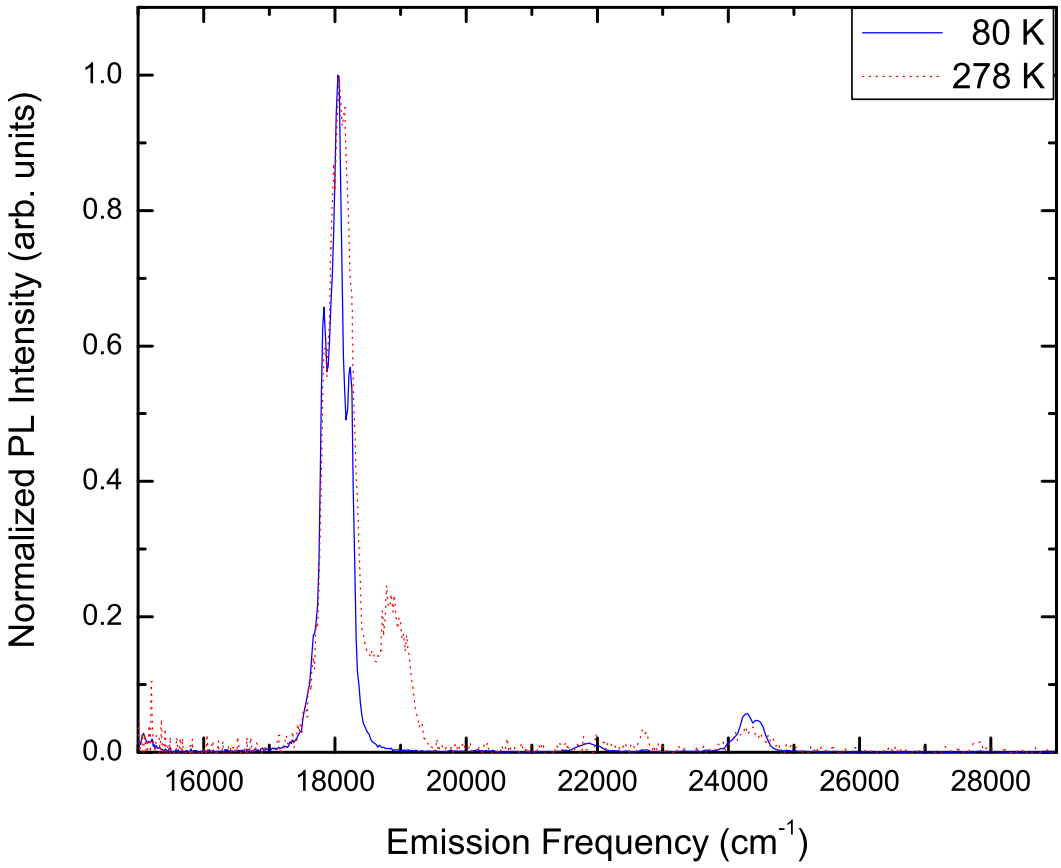

Figure 5.5: Comparison of photoluminescent spectra of CaS:Er^{3+}(0.1%) at 80 K and 278 K.

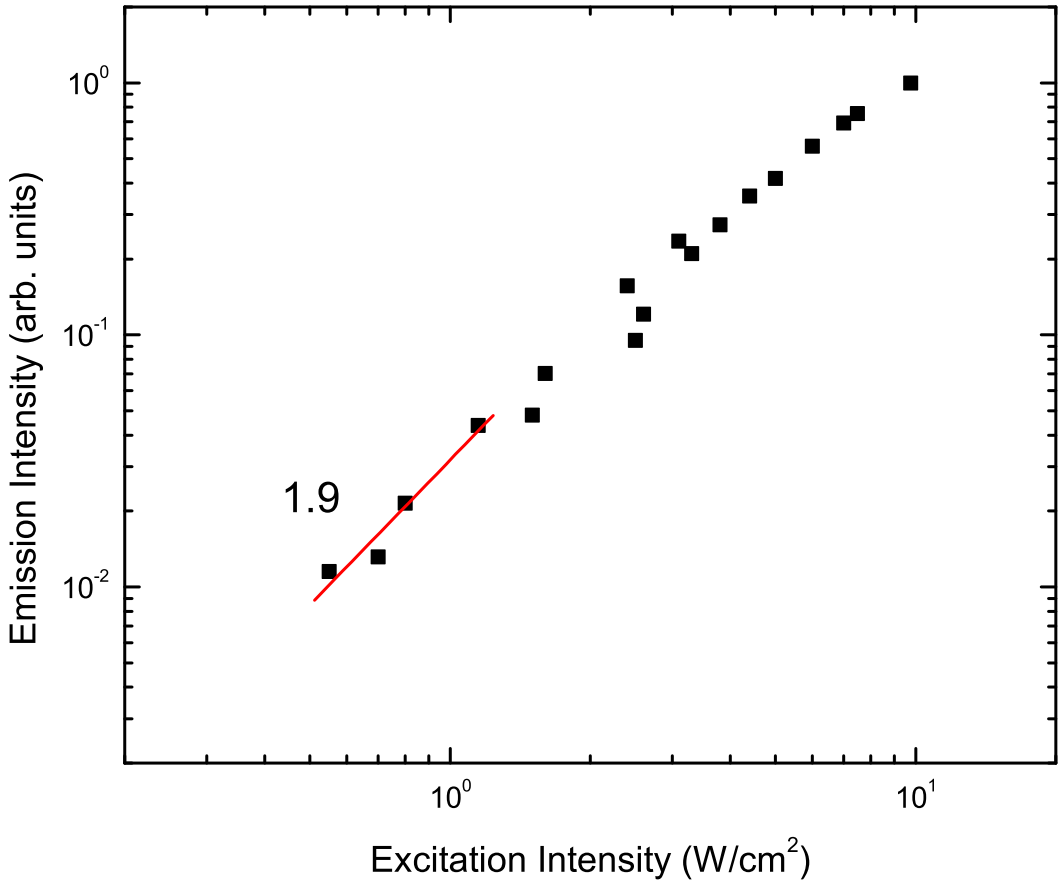

Figure 5.6: Log-log scale plot of excitation intensity at 803.5 nm versus observed PL intensity at 410 nm resulting from the $^2H_{9/2}$ decay to the ground state $^4I_{15/2}$ for CaS:Er^{3+}(0.1%) at room temperature. Line in red is a straight line fit of the data used to calculate the slope at low excitation intensity (labeled on graph).

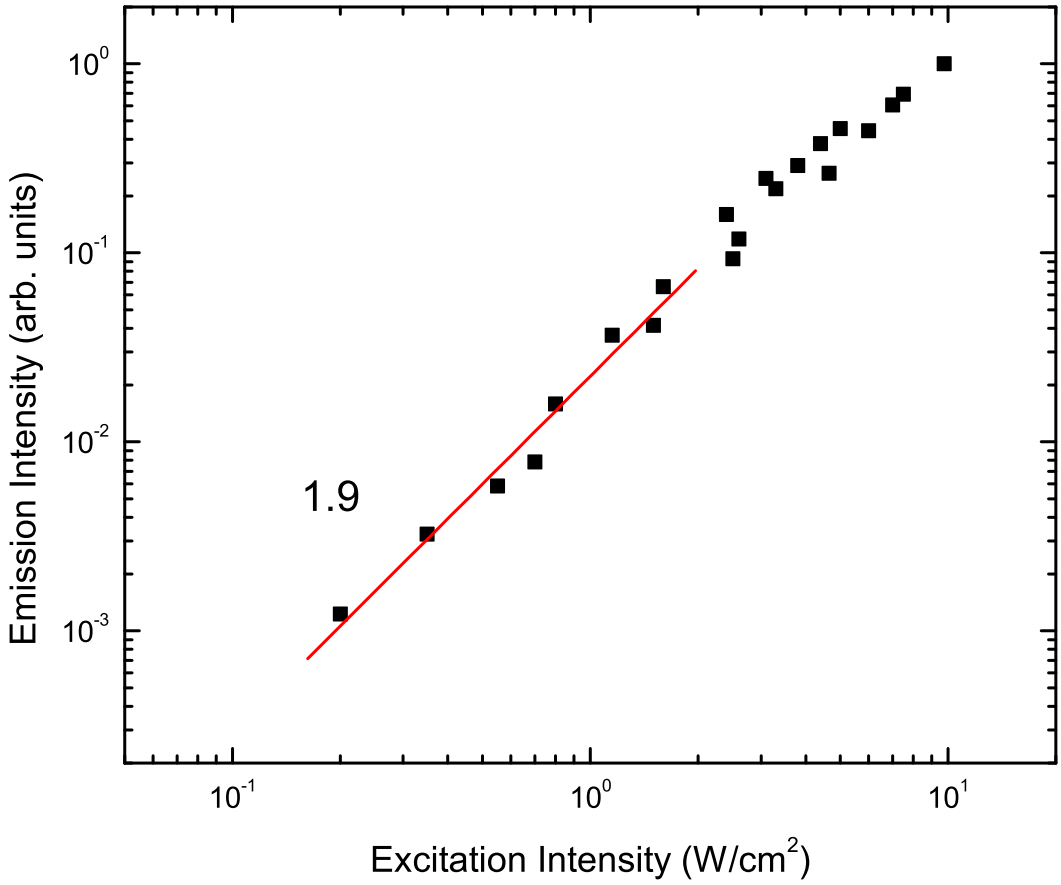

Figure 5.7: Log-log scale plot of excitation intensity at 803.5 nm versus observed PL intensity at 555 nm resulting from the $^4S_{3/2}$ decay to the ground state $^4I_{15/2}$ for CaS:Er^{3+}(0.1%) at room temperature. Line in red is a straight line fit of the data used to calculate the slope at low excitation intensity (labeled on graph).

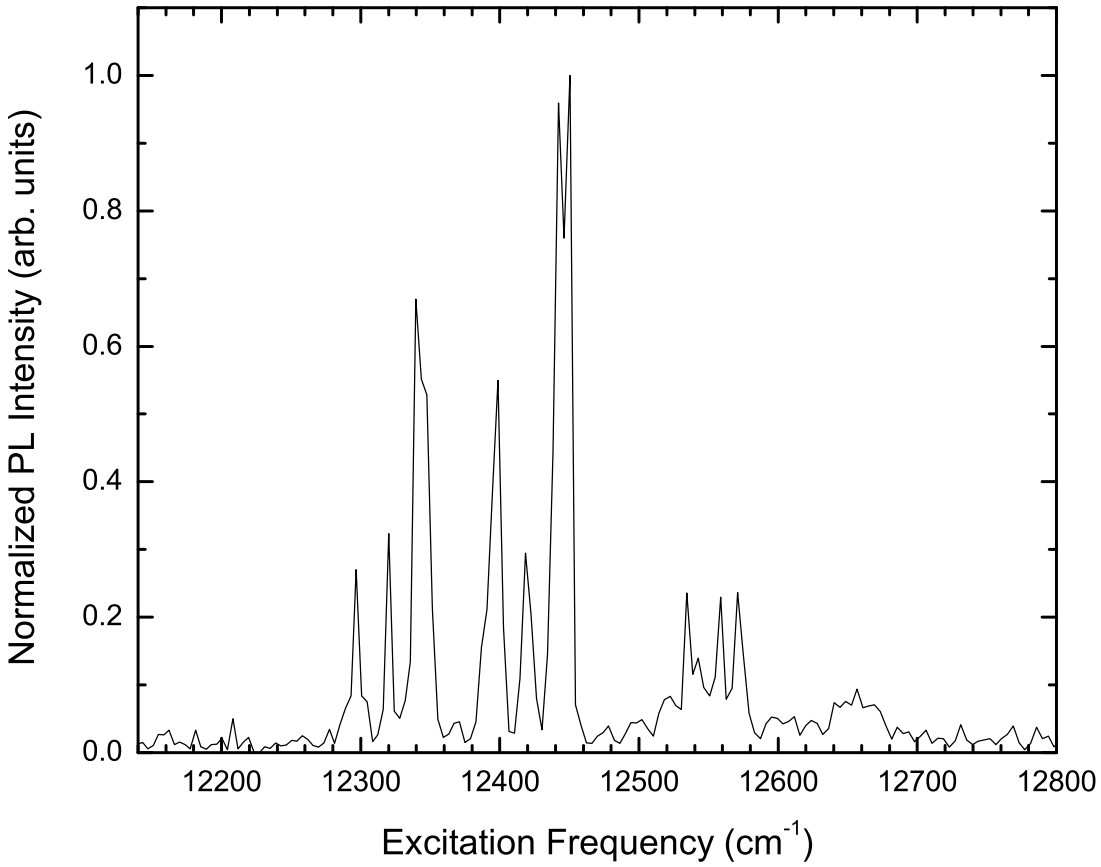

Figure 5.8: Low temperature (77 Kelvin) excitation spectrum of CaS:Er^{3+}(0.1%). Plot shows normalized photoluminescent intensity measured at 555 nm as a function of photoexcitation frequency.

Chapter 6

Near Infrared Measurements

Erbium doped materials have been an integral part of the telecommunications industry since the late 1980s when erbium doped fiber amplifier (EDFA) research was established [61]. The most common telecommunications band, C, operates between 1530 nm and 1565 nm. The band range corresponds to a transmission maximum for the silica-based fibers that carry optical signals over long distances [62].

Erbium doped materials exhibiting a population inversion between the $^4I_{15/2}$ ground state and the first excited state, $^4I_{13/2}$, act as optical amplifiers. They receive communication signals at 1540 nm which are amplified by stimulated emission from the erbium doped material. Since the goal of the population inversion is to establish a large number of ions in the first excited state, energy transfer processes are discouraged by maintaining low doping concentrations. Most EDFAs are low doped materials, ranging from 0.05% to 1.0% [63]. To measure the potential success of CaS:Er^{3+}(0.1%) as a telecommunications material we will need to look for a long radiative lifetime in the $^4I_{13/2}$ state and good thermal stability for that lifetime.

6.1 Spectroscopic Methods

In all measurements, a small amount of sample material in its powder form is packed inside a custom built aluminum sample holder and held in place behind a quartz window. Measurements below room temperature are acquired with the use of an Oxford Optistat Bath Cryostat filled with liquid nitrogen. Measurements above room temperature are obtained

from within a custom built ultra high vacuum (UHV) chamber. Sample temperature is stabilized by an Oxford ITC601 temperature controller and a sample space heat exchanger. All post collection data analysis is performed using the Origin Data Analysis and Graphing software (OriginLabs Co.).

6.1.1 Photoluminescence

For the 1.5 μm photoluminescence study, the room temperature sample was excited by a water cooled 810 nm wavelength diode laser (Spectra Diode Labs, SDL-2482) and driver (SDL-820). The laser output was focused onto the sample with a 200 mm focal length spherical mirror. The collected photoluminescent output was analyzed by Fourier transform infrared (FTIR) spectroscopy using a Bruker (IFS 66V) interferometer. The resulting interferrogram was converted into a frequency based excitation spectrum by the proprietary Bruker software (Opus) using fast Fourier transform (FFT) algorithms. The detector used was a liquid nitrogen cooled germanium detector manufactured by Electro-Optical Systems (G-030-E-LN4) in combination with an Electro-Optical Systems (PS-1) amplifier.

6.1.2 Photoexcitation

In other sulfur containing hosts, like calcium thiogallate and $NaYS_2$ [9, 39], the presence of a ligand to metal charge transfer band has been a useful method for exciting the system. The presence of this LMCT band in the CaS host was investigated through photoexcitation studies. The excitation source, provided by a deuterium lamp, was continuously adjusted from 200 nm to 400 nm by a Cary 14 spectrophotometer. The excitation source was modulated via a chopping wheel operating at a frequency of 30 Hz. The modulated radiation illuminates the sample, resulting in a modulated photoluminescence signal. Comparing the modulation of the emission to the excitation pulse signal allows us to remove much of the unmodulated background noise. The photoluminescent signal was observed through a ZnSe window (500 nm - 22 μm transmission range) by a Hamamatsu R1477 photomultiplier tube

(PMT) with a wavelength response in the range 185 nm - 900 nm, resulting in an overall detection range of 500 nm to 900 nm. The PMT sends the amplified signal to a lock-in amplifier (Stanford Research Systems, SR830) which separates any signal which is in phase with the chopper reference from any out of phase signal. The two components are stored and plotted using the Spectra Operating System software, then later analyzed by Origin.

6.1.3 Radiative Lifetime Detection

Photoexcitation for radiative lifetime spectroscopy is achieved by an argon ion laser (Spectra Physics, Stabilite 2017). The beam is modulated by an optical chopper (Stanford Research Systems, 540 controller) using a custom chopping wheel with a duty cycle of 0.25 6.1. The beam is focused to the plane of the chopper in an effort to reduce the rise and fall time of the pulse. The sample is contained within an Oxford Optistat bath cryostat, filled with liquid nitrogen.

The photoluminescent emission is collected and filtered with a combination of filters (2.0 mm thick silicon, and 5.0 mm thick Corning 4784) which attenuate any stray light outside the window of 5000 cm^{-1} to 7000 cm^{-1}. The signal is detected by a nitrogen cooled germanium detector (Electro-Optical Systems, G-030-E-LN4) with a bandwidth of 300 Hz. A portion of the excitation beam is reflected by a thin glass slide and focused on a silicon photodiode detector (Thor Labs, DET 210). The output current is converted into a voltage signal and used as a reference. Both reference signal and emission signal are sent to an oscilloscope (Tektronix TDS 460A). The reference signal is analyzed and used as a trigger for the purpose of averaging multiple emission scans together. The averaged time decay of the photoluminescent signal is recorded, then analyzed using Origin.

6.2 Results

The observed room temperature photoluminescent emission shown in figure 6.2 for the NIR is typical for an erbium doped phosphor. The sharp peaks indicative of $f - f$ transitions are

centered at 6500 cm^{-1} and range from 6400 cm^{-1} to 6620 cm^{-1}. While the small multiplet at 6600 cm^{-1} lies outside the range of the telecommunications band C, the rest of the emission peaks are within range and the maximum peak matches the desired emission wavelength of 1540 nm.

The LMCT band for the sample (figure 6.3) is centered at 33500 cm^{-1} and spans from 28000 cm^{-1} to 37000 cm^{-1}. The small peak at 26000 cm^{-1} is the only visible f-f transition and matches the expected energy of the $^4G_{11/2}$ state. Overall, the excitation spectrum is similar to the spectrum reported by Garcia for erbium doped thiogallates [40] and confirms the presence of a LMCT band. The frequency range for the band dictates our choice of the argon laser with its 28490 cm^{-1} output as an excitation source for the lifetime measurements.

At 77 Kelvin, the transient emission of the $^4I_{13/2} \rightarrow ^4I_{15/2}$ transition can be described by a single exponential with a relaxation time constant of 10.0 ms (see figure 6.4). This value is typical for EDFA materials. As the sample temperature is increased, the radiative lifetime decreases slightly, but remains stable beyond room temperature, with an overall reduction of 10% from 77 Kelvin to 475 Kelvin (see figure 6.5). While the long lifetime and good thermal stability are encouraging, these properties are similar to currently available materials.

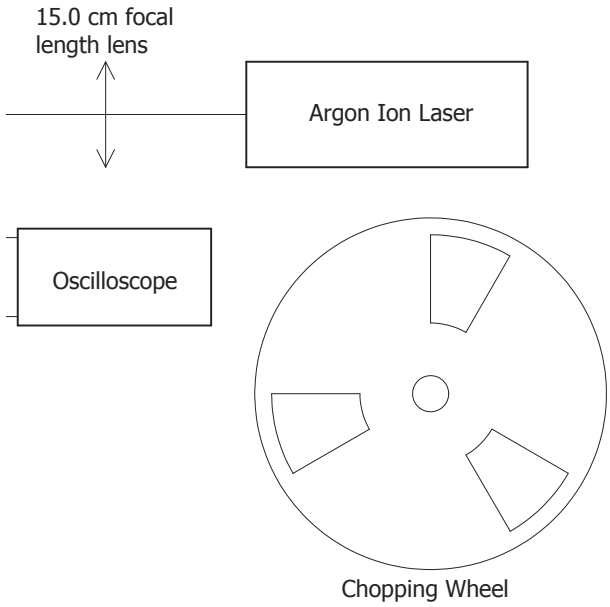

Figure 6.1: Schematic diagram of PL decay time measurements, with custom chopping wheel design. Wheel slits are 30° wide and provide a pulse width equal to 25% of the pulse period.

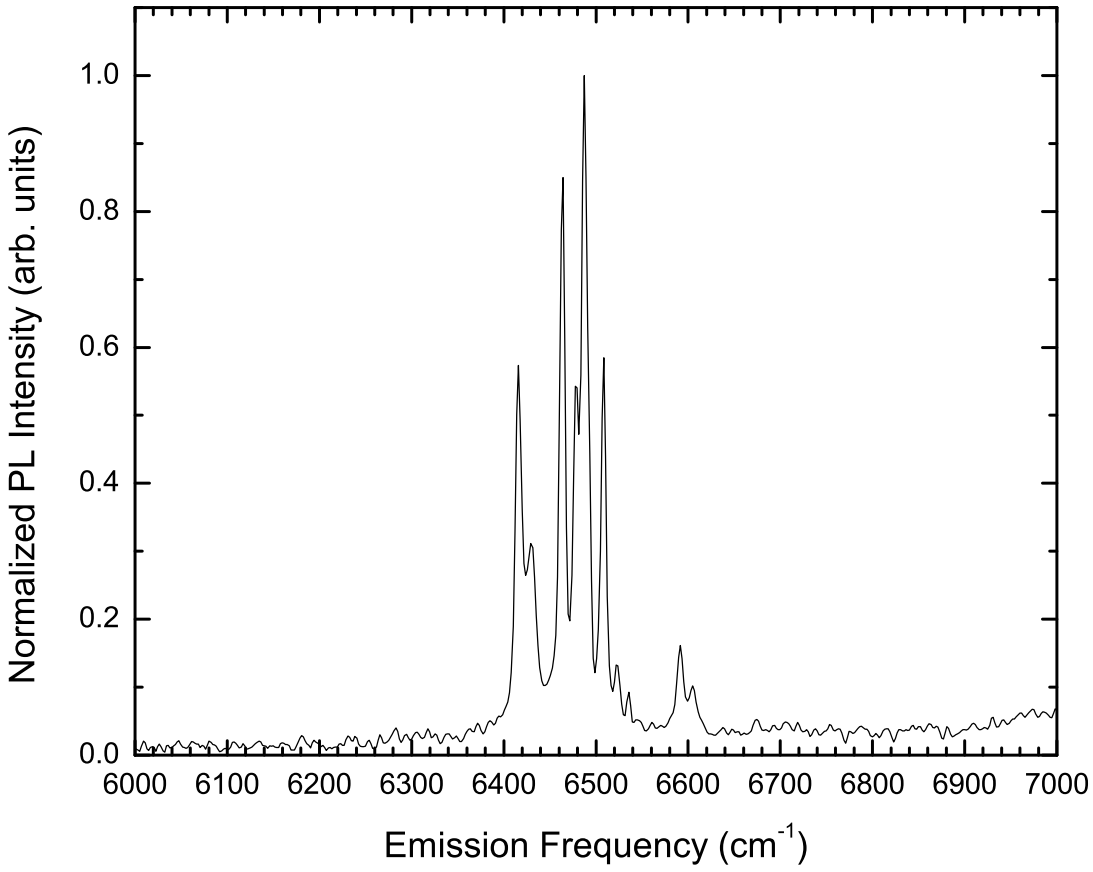

Figure 6.2: Room temperature emission spectrum of CaS:Er^{3+}(0.1%) obtained through FTIR spectroscopy of 810 nm excitation.

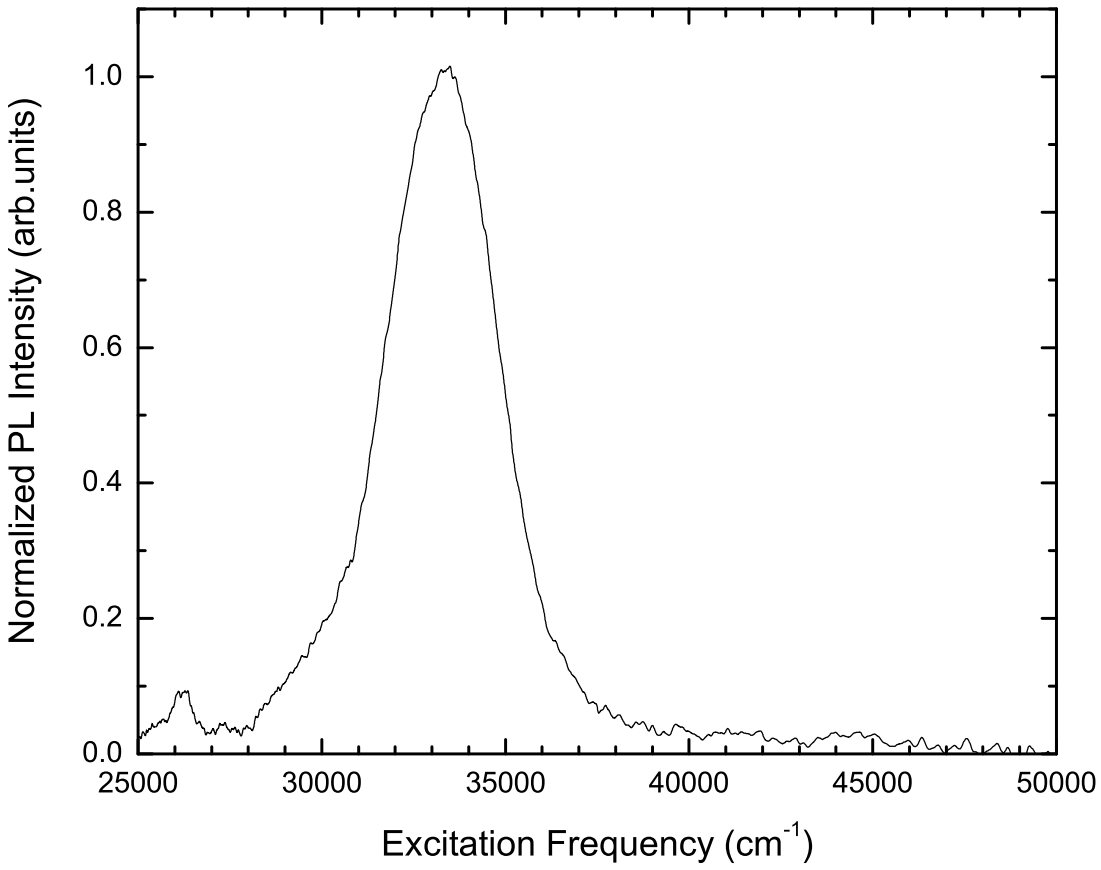

Figure 6.3: Room temperature PL excitation spectrum of CaS:Er^{3+}(0.1%) based on PL emission ranging from 500 nm to 900 nm.

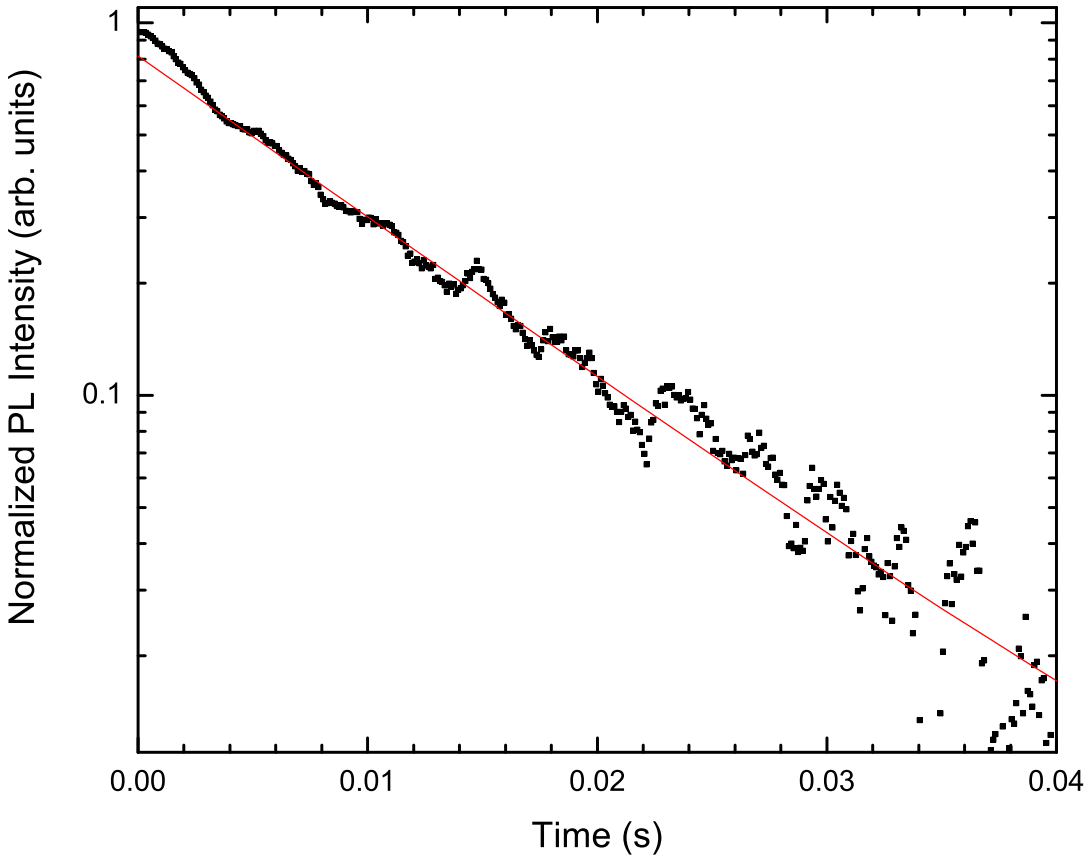

Figure 6.4: Low temperature (77 Kelvin) time decay of PL emission from CaS:Er^{3+}(0.1%) $^4I_{13/2}$ via LMCT excitation. The red line is an exponential decay curve fit to the data.

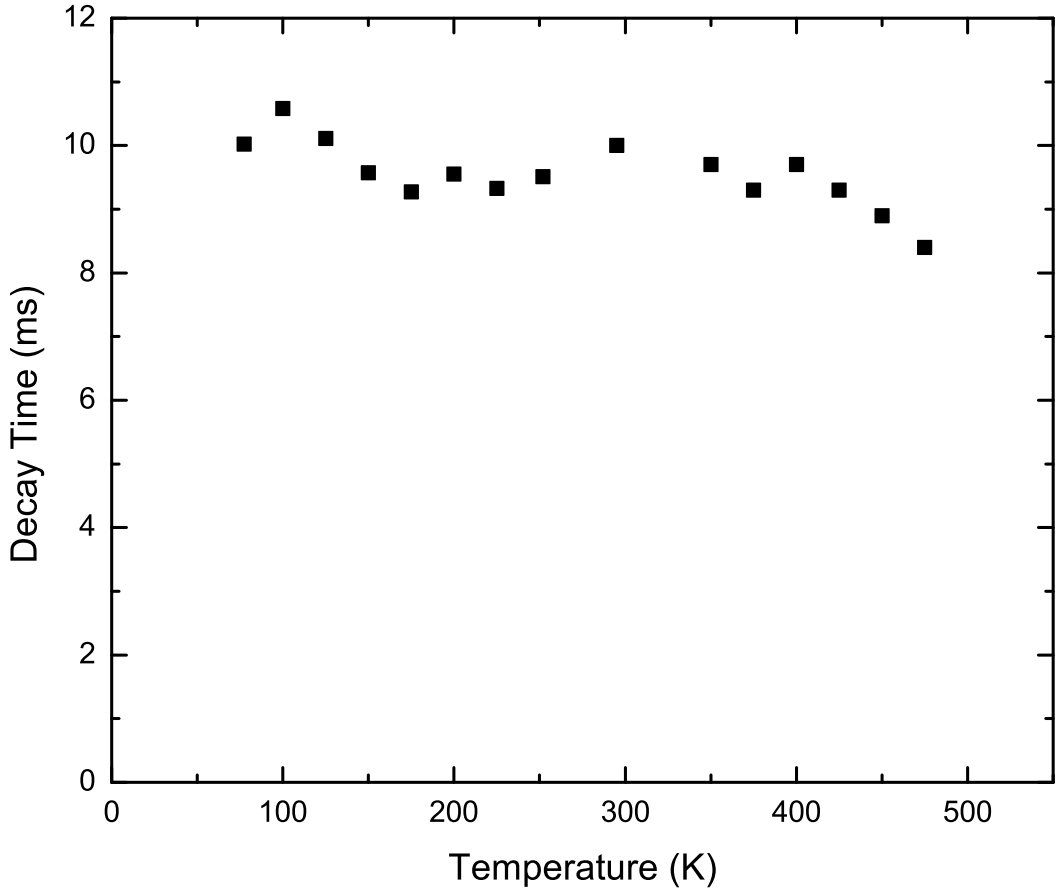

Figure 6.5: Decay time for $^4I_{13/2}$ state of CaS:Er^{3+}(0.1%) as a function of sample temperature.

Chapter 7

Conclusion

The goal of this study is to investigate a phosphor for medical applications that takes advantage of the transmission window of human tissue and which can easily be functionalized to organic delivery systems. The host and dopant combination of calcium sulfide with erbium exhibits several promising properties. The excitation frequency occurs in a low energy region of the electromagnetic spectrum transmissive through human tissue. The emission occurs in the target range which is safe for surrounding tissue. The potential to couple with other molecular systems with thiol functional groups is promising, but the inefficiency of the upconversion process, especially at low excitation intensity, is a concern.

Additional research was performed to investigate basic properties related to the NIR region. A 10.0 millisecond lifetime at 77 Kelvin was observed for 1.5 μm emission, comparable to other sulfide-containing hosts. The relaxation time remains stable above room temperature indicating a purely radiative relaxation.

Future research could be done to increase the efficiency either by adjusting the dopant ion concentration or by adding a sensitizer like Yb^{3+}. It should be noted, however, that for small particles the addition of Yb^{3+} could introduce a loss channel as a result of energy transfer to surface hydroxyl (-OH) groups and other surface quenching effects [64]. In addition, the heating temperature and duration should be further evaluated to minimize particle size. We have provided the data required to evaluate the efficacy of erbium doped calcium sulfide for medical treatments.

Bibliography

[1] J. Emsley, *Nature's building blocks: an A-Z guide to the elements*, Oxford University Press, 2001.

[2] M. E. Daub and M. Ehrenshaft, Annual Review of Phytopathology **38**, 461 (2000).

[3] K. Licha and C. Olbrich, Advanced Drug Delivery Reviews **57**, 1087 (2005), Non-Invasive Spectroscopic and Imaging Techniques in Drug Delivery.

[4] D. K. Chatterjee, A. J. Rufaihah, and Y. Zhang, Biomaterials **29**, 937 (2008).

[5] R. Goncalves et al., Optical Materials **25**, 131 (2004).

[6] R. Van Deun, P. Nockemann, C. Gorller-Walrand, and K. Binnemans, Chemical Physics Letters **397**, 447 (2004).

[7] T. Feuchter, E. Mwarania, J. Wang, L. Reekie, and J. Wilkinson, IEEE Photonics Technology Letters **4**, 542 (1992).

[8] A. Polman, Journal of Applied Physics **82**, 1 (1997).

[9] P. Gerner and H. U. Güdel, Chemical Physics Letters **413**, 105 (2005).

[10] N. Bloembergen, Physical Review Letters **2**, 84 (1959).

[11] T. Förster, Annalen der Physik **437**, 55 (1948).

[12] D. L. Dexter, The Journal of Chemical Physics **21**, 836 (1953).

[13] F. Auzel, Comptes Rendus Hebdomadaires des Seances de l Academie des Sciences Serie B **262**, 1016 (1966).

[14] F. Auzel and Deutschb.O, Zeitschrift fur Naturforschung Part A-Astrophysik Physik und Physikalische Chemie **A 24**, 1562 (1969).

[15] F. Auzel, Proceedings of the IEEE **61**, 758 (1973).

[16] V. Ovsyanki and P. Feofilov, JETP Letters-USSR **3**, 322 (1966).

[17] Ovsyanki.VV and P. Feofilov, Izvestiya Akademii nauk SSSR Seriya Fizicheskaya **37**, 262 (1973).

[18] M.-F. Joubert, Optical Materials **11**, 181 (1999).

[19] R. Scheps, Progress in Quantum Electronics **20**, 271 (1996).

[20] F. Auzel, Chemical Reviews **104**, 139 (2004).

[21] G. Fowles, *Introduction to Modern Optics*, Dover Publications Inc., New York, second edition, 1975.

[22] P. Golding, S. Jackson, T. King, and M. Pollnau, Physical Review B **62**, 856 (2000).

[23] X. Wang et al., Journal of Physical Chemistry B **108**, 18408 (2004).

[24] F. Goutaland, Y. Ouerdane, A. Boukenter, and G. Monnom, Journal of Alloys and Compounds **275**, 276 (1998).

[25] S. Heer, K. Kompe, H. Güdel, and M. Haase, Advanced Materials **16**, 2102 (2004).

[26] M. Hehlen, N. Cockroft, T. Gosnell, and A. Bruce, Physical Review B **56**, 9302 (1997).

[27] K. Kramer et al., Chemistry of Materials **16**, 1244 (2004).

[28] J. Hutchinson and T. Allik, Applied Physics Letters **60**, 1424 (1992).

[29] R. Page et al., Journal of the Optical Society of America B-Optical Physics **15**, 996 (1998).

[30] R. Orbach, Relaxation and energy transfer, in *Optical Properties of Ions in Solids*, pages 355–399, New York, 1974, Plenum Press.

[31] N. J. Cockroft, G. D. Jones, and R. W. G. Syme, Journal of Luminescence **43**, 275 (1989).

[32] S. R. Lüthi, M. P. Hehlen, T. Riedener, and H. U. Güdel, Journal of Luminescence **76-77**, 447 (1998), Proceedings of the Eleventh International Conference on Dynamical Processes in Excited States of Solids.

[33] U. Schäfer, J. Neukum, N. Bodenschatz, and J. Heber, Journal of Luminescence **60-61**, 633 (1994), International Conference on Luminescence.

[34] J. B. Gruber, W. F. Krupke, and J. M. Poindexter, The Journal of Chemical Physics **41**, 3363 (1964).

[35] G. Dieke and H. Crosswhite, Applied Optics **2**, 675 (1963).

[36] S. R. Lüthi, M. Pollnau, H. U. Güdel, and M. P. Hehlen, Phys. Rev. B **60**, 162 (1999).

[37] J. Rubin, A. Brenier, R. Moncorge, and C. Pedrini, Journal of Luminescence **36**, 39 (1986).

[38] L. M. Fortes et al., Optical Materials **29**, 503 (2007).

[39] A. Georgobiani et al., Journal of the Electrochemical Society **148**, H167 (2001).

[40] A. Garcia, C. Fouassier, and P. Dougier, Journal of the Electrochemical Society **129**, 2063 (1982).

[41] W. Lehmann, Journal of Luminescence **5**, 87 (1972).

[42] J. Brightwell, B. Ray, and C. Buckley, Journal of Crystal Growth **59**, 210 (1982), Proceedings of the International Conference on II-VI Compounds.

[43] A. N. Gruzintsev, V. T. Volkov, and A. N. Pronin, Journal of Crystal Growth **110**, 429 (1991).

[44] A. N. Gruzintsev, V. T. Volkov, and A. N. Pronin, Journal of Crystal Growth **117**, 975 (1992).

[45] F. Okamoto and K. Kato, Journal of the Electrochemical Society **130**, 432 (1983).

[46] W. Lehmann, Journal of the Electrochemical Society **117**, 1389 (1970).

[47] W. Lehmann and F. Ryan, Journal of the Electrochemical Society **118**, 477 (1971).

[48] P. Patnaik, *Handbook of Inorganic Chemicals*, McGraw-Hill, first edition, 2002.

[49] C. for Computational Materials Science of the United States Naval Research Laboratory, Crystal lattice structures web page, http://cst-www.nrl.navy.mil/lattice/.

[50] K. Qiu, T. Mattisson, B.-M. Steenari, and O. Lindqvist, Thermochimica Acta **298**, 87 (1997).

[51] M. Pollnau, D. R. Gamelin, S. R. Lüthi, H. U. Güdel, and M. P. Hehlen, Phys. Rev. B **61**, 3337 (2000).

[52] K. König, T. W. Becker, P. Fischer, I. Riemann, and K.-J. Halbhuber, Opt. Lett. **24**, 113 (1999).

[53] B. Chance, M. Cope, E. Gratton, N. Ramanujam, and B. Tromberg, Review of Scientific Instruments **69**, 3457 (1998).

[54] B. Henderson and G. F. Imbusch, *Optical Spectroscopy of Inorganic Solids*, Oxford Science Publications, 1989.

[55] J. M. Khosrofian and B. A. Garetz, Appl. Opt. **22**, 3406 (1983).

[56] J. B. Fishkin, O. Coquoz, E. R. Anderson, M. Brenner, and B. J. Tromberg, Appl. Opt. **36**, 10 (1997).

[57] B. Tromberg et al., Philosophical Transactions of the Royal Society of London Series B-Biological Sciences **352**, 661 (1997).

[58] L. O. Svaasand, On the physical rationale of photodynamic therapy, in *Future Directions and Application in Photodynamic Therapy*, edited by C. J. Gomer, pages 233–248, SPIE, 1990.

[59] M. A. Trelles et al., Journal of the American Academy of Dermatology **54**, 282 (2006).

[60] W. R. Chen et al., Cancer Letters **88**, 15 (1995).

[61] E. Desurvire, Physics Today **47**, 20 (1994).

[62] H. J. R. Dutton, *Understanding Optical Communications*, IBM Redbooks, first edition, 1998.

[63] A. Polman, Journal of Applied Physics **82**, 1 (1997).

[64] J. K. Krebs, *Luminescent Properties of Trivalent Ytterbium Ions in Sol-Gel Produced Alumina*, PhD thesis, University of Georgia, 2000.